Journal of Computational Physics 498 (2024) 112705

Contents lists available at ScienceDirect

Journal of Computational Physics

journal homepage: www.elsevier.com/locate/jcp

Computation of unsteady electromagnetic scattering about 3D complex bodies in free space with high-order difference potentials ☆

Sergey Petropavlovsky [a], Semyon Tsynkov [b,*], Eli Turkel [c]

[a] HSE University, Moscow 101000, Russia
[b] Department of Mathematics, North Carolina State University, Box 8205, Raleigh, NC 27695, USA
[c] School of Mathematical Sciences, Tel Aviv University, Ramat Aviv, Tel Aviv 69978, Israel

ARTICLE INFO

Keywords:
Maxwell's equations
CAD surface with piece-wise parameterization
Calderon's boundary equations with projections
High-order compact schemes on Cartesian grids
Non-conforming scattering shapes
Huygens' principle

ABSTRACT

We extend the previously developed high-order accurate method for acoustic scattering to electromagnetic scattering, i.e., from the scalar setting to a vector setting. First, the governing Maxwell's equations are reduced from their original first-order form to a system of second-order wave equations for the individual Cartesian components of electromagnetic field. In free space, these wave equations are uncoupled. Yet at the boundary of the scatterer, the variables that they govern (i.e., Cartesian field components) remain fully coupled via the boundary conditions that account for the specific scattering mechanism. Next, the wave equations are equivalently replaced with Calderon's boundary equations with projections obtained using the method of difference potentials and a compact high-order accurate scheme. The Calderon's boundary equations are combined with the boundary conditions and the overall system is solved by least squares. The resulting vector methodology (electromagnetic) inherits many useful properties of the scalar one (acoustic). In particular, it offers sub-linear computational complexity, does not require any special treatment of the artificial outer boundary, and has the capacity to solve multiple similar problems at a low individual cost per problem. We demonstrate the performance of the new method by computing the scattering of a given impinging wave about a double-cone hypersonic shape.

1. Introduction

1.1. Background

In our previous work [1–3], we developed a high-order accurate numerical method that employs Calderon's operators and difference potentials for computing the scattering of time-dependent acoustic waves about general shapes in three space dimensions. The acoustic field is governed by the second-order wave (d'Alembert) equation. The surface of the scatterer is defined via CAD and represented using piece-wise parameterization by splines on a set of non-overlapping patches. The method uses Cartesian grids but

☆ Work supported by the US–Israel Binational Science Foundation (BSF) under grant # 2020128.
* Corresponding author.
E-mail addresses: spetropavlovsky@gmail.com (S. Petropavlovsky), tsynkov@math.ncsu.edu (S. Tsynkov), turkel@tauex.tau.ac.il (E. Turkel).
URLs: https://stsynkov.math.ncsu.edu (S. Tsynkov), http://www.math.tau.ac.il/~turkel/ (E. Turkel).

https://doi.org/10.1016/j.jcp.2023.112705
Received 16 August 2023; Received in revised form 4 December 2023; Accepted 4 December 2023

Available online 12 December 2023

allows for general non-conforming geometries with no deterioration of either accuracy or stability. It explicitly takes into account the (strong) Huygens' principle and thus performs uniformly well over arbitrarily long computation times. Moreover, it offers the exact treatment of artificial outer boundaries and sub-linear computational complexity with respect to the grid dimension.

1.2. Governing equations

In the current work, we extend the method of [1–3] from acoustics to Maxwell's equations so that its advantageous properties identified in Section 1.1 are preserved. We study the scattering of time-dependent electromagnetic waves in free space about three-dimensional obstacles of a given shape with given properties of the surface. The impinging wave is assumed known. It propagates through free space (vacuum) and bounces off the scatterer. Our objective is to compute the scattered electromagnetic field.

The propagation is governed by the homogeneous Maxwell's equations of electrodynamics:

$$\begin{aligned} &\frac{1}{c}\frac{\partial \boldsymbol{H}}{\partial t} + \operatorname{curl}\boldsymbol{E} = \boldsymbol{0}, \qquad \operatorname{div}\boldsymbol{H} = 0, \\ &\frac{1}{c}\frac{\partial \boldsymbol{E}}{\partial t} - \operatorname{curl}\boldsymbol{H} = \boldsymbol{0}, \qquad \operatorname{div}\boldsymbol{E} = 0, \end{aligned} \tag{1}$$

where $\boldsymbol{E}$ is the electric field, $\boldsymbol{H}$ is the magnetic field, and c is the speed of light, see [4]. The two unsteady equations in (1) are the Faraday law and Ampère law. They form a first-order hyperbolic system supplemented by two steady-state equations, the Gauss law for magnetism and Gauss law for electricity.

By taking the divergence of each unsteady equation of (1), we obtain:

$$\frac{\partial \operatorname{div}\boldsymbol{H}}{\partial t} = 0 \quad \text{and} \quad \frac{\partial \operatorname{div}\boldsymbol{E}}{\partial t} = 0. \tag{2}$$

Equations (2) imply that as long as $\operatorname{div}\boldsymbol{H} = 0$ and $\operatorname{div}\boldsymbol{E} = 0$ at $t = 0$, the fields $\boldsymbol{H}$ and $\boldsymbol{E}$ will remain solenoidal (i.e., divergence free) for all $t > 0$. Therefore, as long as the Gauss laws hold for the initial data, they will hold for all future moments of time as well.

By taking the time derivative of the Faraday law in (1), substituting $\frac{\partial}{\partial t}\operatorname{curl}\boldsymbol{E}$ from the Ampère law, employing the identity $\operatorname{curl}\operatorname{curl}\boldsymbol{H} = -\Delta\boldsymbol{H} + \operatorname{grad}\operatorname{div}\boldsymbol{H}$, and using $\operatorname{div}\boldsymbol{H} = 0$, we arrive at the homogeneous vector wave (d'Alembert) equation for the magnetic field $\boldsymbol{H}$:

$$\frac{1}{c^2}\frac{\partial^2 \boldsymbol{H}}{\partial t^2} - \Delta\boldsymbol{H} = \boldsymbol{0}. \tag{3a}$$

A very similar argument yields the homogeneous vector wave equation for $\boldsymbol{E}$:

$$\frac{1}{c^2}\frac{\partial^2 \boldsymbol{E}}{\partial t^2} - \Delta\boldsymbol{E} = \boldsymbol{0}. \tag{3b}$$

The two wave equations (3a) and (3b) are independent. Moreover, if the fields $\boldsymbol{E}$ and $\boldsymbol{H}$ are represented by their Cartesian components in $\mathbb{R}^3$, then each of the equations (3a) or (3b) further reduces to three independent scalar wave equations for those components. Yet the independence holds only in free space. When electromagnetic waves interact with obstacles, the fields governed by the vector wave equations (3a) and (3b), as well as their individual Cartesian components, become coupled through the boundary conditions (Section 1.3).

Let us also emphasize that, the derivation of the wave equations (3) from Maxwell's equations (1) explicitly takes into account that $\operatorname{div}\boldsymbol{H} = 0$ and $\operatorname{div}\boldsymbol{E} = 0$. Hence, every solution of Maxwell's equations (1), which is divergence free by definition, satisfies equations (3). This does not mean, however, that every solution of equations (3) is automatically divergence free. Indeed, by applying the divergence operator to (3a) and (3b) we conclude that each of the two quantities, $\operatorname{div}\boldsymbol{H}$ and $\operatorname{div}\boldsymbol{E}$, satisfies its own scalar wave equation:

$$\frac{1}{c^2}\frac{\partial^2 \operatorname{div}\boldsymbol{H}}{\partial t^2} - \Delta\operatorname{div}\boldsymbol{H} = 0 \quad \text{and} \quad \frac{1}{c^2}\frac{\partial^2 \operatorname{div}\boldsymbol{E}}{\partial t^2} - \Delta\operatorname{div}\boldsymbol{E} = 0. \tag{4}$$

Having $\operatorname{div}\boldsymbol{H} = 0$ and $\operatorname{div}\boldsymbol{E} = 0$ at $t = 0$ is not sufficient to guarantee that $\operatorname{div}\boldsymbol{H} = 0$ and $\operatorname{div}\boldsymbol{E} = 0$ for all $t > 0$, as in (2). Additional initial and boundary conditions are required.

1.3. Initial and boundary conditions for Maxwell's equations in second-order form

Let $\Omega \subset \mathbb{R}^3$ be a bounded domain in space that we interpret as the scattering body. Its boundary $\partial\Omega$ is the scattering surface. Our goal is to solve equations (3) for the scattered field on the complementary domain $\mathbb{R}^3\backslash\Omega$ for $t \in [0, T]$, where $T > 0$ is the final moment of time which can be arbitrary. Accordingly, initial conditions need to be specified on $\mathbb{R}^3\backslash\Omega$ at $t = 0$ and boundary conditions need to be specified on $\partial\Omega$ for $t \in [0, T]$.

The boundary conditions on the lateral boundary $\Gamma \equiv \partial\Omega \times [0, T]$ should account for the specific physical mechanism of scattering on the surface. In most cases though, scattering is accompanied by transmission. This means that the impinging wave is partially reflected off the scatterer back to the exterior domain $\mathbb{R}^3\backslash\Omega$ and partially propagates inwards, i.e., into the interior domain Ω. This is very typical when, for example, the scattering material is a dielectric, see [5, Sections 7, 76, and 86]. Then, the transmission/scattering problem cannot be solved only on $\mathbb{R}^3\backslash\Omega$. It rather has to be solved it its entirety, i.e., simultaneously on $\mathbb{R}^3\backslash\Omega$ and Ω, with the appropriate interface conditions on Γ taken into account.

If the scattering material is a conductor (metal), then the "penetration depth" of the impinging electromagnetic field into the material often appears small compared to the wavelength in vacuum. In that case, the exterior scattering problem can be solved separately, i.e., without considering the interior transmission. In doing so, the following impedance boundary condition holds on the surface $\partial\Omega$ (see [5, Section 87], as well as [6,7]):

$$\hat{\boldsymbol{E}}_\tau = \zeta \hat{\boldsymbol{H}}_\tau \times \boldsymbol{n}. \tag{5}$$

In formula (5), $\hat{\boldsymbol{E}}_\tau$ and $\hat{\boldsymbol{H}}_\tau$ denote the tangential components of the electric and magnetic field in the frequency domain, respectively, $\boldsymbol{n}$ is the interior normal to $\partial\Omega$, and ζ is the surface impedance, which is a complex-valued quantity that depends on the impinging frequency and material characteristics: electric conductivity and magnetic permeability. Boundary condition (5) holds for a broad range of impinging frequencies, from very long radio waves to microwaves and all the way up to infrared. In the time domain, the boundary condition (5) becomes nonlocal and involves a convolution product in time.

If the scattering material is a perfect electric conductor (PEC), then the electromagnetic field does not penetrate into the material at all. Accordingly, the surface impedance vanishes, $\zeta = 0$, and the boundary condition (5) simplifies further:

$$\boldsymbol{E}_\tau = \boldsymbol{0}. \tag{6}$$

Note that, the boundary condition (6) can be considered directly in the time domain. It is very important that unlike in (5), there is no coupling between the electric and magnetic field at the boundary. Consequently, the wave equation (3b) subject to boundary condition (6) can be solved separately, i.e., without having to solve for the magnetic field. Nonetheless, the individual components of the electric field remain coupled at the boundary by the boundary condition (6). Moreover, boundary condition (6) alone is not sufficient to guarantee uniqueness of the solution to the wave equation (3b). The latter has to be supplemented by another boundary condition on Γ, as well as the initial conditions on $\mathbb{R}^3\backslash\Omega$.

The overall electric field on $\mathbb{R}^3\backslash\Omega$ is the sum of the impinging and scattered fields: $\boldsymbol{E} = \boldsymbol{E}^{\text{imp}} + \boldsymbol{E}^{\text{sc}}$, where $\boldsymbol{E}^{\text{imp}}$ is known and $\boldsymbol{E}^{\text{sc}}$ is to be computed. With no loss of generality, the initial moment of time $t = 0$ can be taken when the impinging wave first hits the scatterer. This implies that the initial conditions can be chosen homogeneous. Indeed, there will be no scattered field anywhere on $\mathbb{R}^3\backslash\Omega$ at $t = 0$. Since Maxwell's equations (1) form a first-order system, the only physical quantity that needs to be provided at $t = 0$ is the scattered field itself: $\boldsymbol{E}^{\text{sc}} = \boldsymbol{0}$ (same for magnetic field if coupled). For the second-order formulation (3), the first time derivative also needs to be specified: $\frac{\partial \boldsymbol{E}^{\text{sc}}}{\partial t} = \boldsymbol{0}$. This derivative is zero because the propagation speed is finite and consequently, the scattered field $\boldsymbol{E}^{\text{sc}}$ is zero on $\mathbb{R}^3\backslash\Omega$ not only at $t = 0$ but at any infinitesimally small positive moment of time as well.

As both the field and its derivative $\frac{\partial}{\partial t}$ are equal to zero at $t = 0$, the field divergence and its first derivative with respect to time are also zero. Yet the scalar wave equations (4) on $\mathbb{R}^3\backslash\Omega \times [0, T]$, subject to homogeneous initial conditions, still do not guarantee zero divergence everywhere. For that, we additionally need to require that the divergence be zero at the boundary. In the case where the electric and magnetic field fully decouple due to the PEC boundary condition (6), we require that $\operatorname{div}\boldsymbol{E} = 0$ on $\partial\Omega$ for $t \in [0, T]$. In the case where the electric and magnetic field satisfy the impedance boundary condition (5) (rather than the simpler PEC boundary condition (6) for the electric field only), one needs to solve for both fields, i.e., solve both wave equations (3) simultaneously, and in addition to the zero divergence boundary condition for the electric field impose zero divergence boundary condition for the magnetic field: $\operatorname{div}\boldsymbol{H} = 0$ on $\partial\Omega$ for $t \in [0, T]$.

When solving for the electric field only, we assume with no loss of generality that $\operatorname{div}\boldsymbol{E}^{\text{imp}} = 0$. Then, we have $\operatorname{div}\boldsymbol{E}^{\text{sc}} = 0$. The latter relation provides an additional boundary condition to supplement (6). In turn, boundary condition (6) can be recast as

$$\boldsymbol{E}^{\text{sc}}_\tau\Big|_\Gamma = -\boldsymbol{E}^{\text{imp}}_\tau\Big|_\Gamma. \tag{6$'$}$$

Altogether, the exterior electromagnetic scattering problem about a PEC surface consists of solving the vector wave equation (3b) for the scattered field $\boldsymbol{E}^{\text{sc}}$ on $\mathbb{R}^3\backslash\Omega$, subject to the homogeneous initial conditions, boundary condition (6$'$), and additional boundary condition $\operatorname{div}\boldsymbol{E}^{\text{sc}} = 0$ on $\Gamma = \partial\Omega \times [0, T]$. The solution $\boldsymbol{E}^{\text{sc}}$ is driven by the tangential component $\boldsymbol{E}^{\text{imp}}_\tau$ of the impinging electric field that is assumed given on Γ:

$$\frac{1}{c^2}\frac{\partial^2 \boldsymbol{E}^{\text{sc}}}{\partial t^2} - \Delta \boldsymbol{E}^{\text{sc}} = \boldsymbol{0} \quad \text{on} \quad \mathbb{R}^3\backslash\Omega \times [0, T], \tag{7a}$$

$$\boldsymbol{E}^{\text{sc}}_\tau = -\boldsymbol{E}^{\text{imp}}_\tau \quad \text{on} \quad \Gamma, \tag{7b}$$

$$\operatorname{div}\boldsymbol{E}^{\text{sc}} = 0 \quad \text{on} \quad \Gamma, \tag{7c}$$

$$\boldsymbol{E}^{\text{sc}}\big|_{t=0} = \boldsymbol{0}, \quad \frac{\partial \boldsymbol{E}^{\text{sc}}}{\partial t}\bigg|_{t=0} = \boldsymbol{0} \quad \text{on} \quad \mathbb{R}^3\backslash\Omega. \tag{7d}$$

The unknown scattered field $\boldsymbol{E}^{\text{sc}}$ governed by the wave equation (7a) consists of three scalar components on $\mathbb{R}^3$. Accordingly, three scalar boundary conditions are required for uniqueness. The Dirichlet-type boundary condition (7b) provides only two scalar conditions. Indeed, if $\boldsymbol{\tau}_1$ and $\boldsymbol{\tau}_2$ are two orthogonal unit vectors tangent to the surface $\partial\Omega$ at a given point, then (7b) is equivalent to two scalar relations: $\boldsymbol{E}^{\text{sc}} \cdot \boldsymbol{\tau}_1 = -\boldsymbol{E}^{\text{imp}} \cdot \boldsymbol{\tau}_1$ and $\boldsymbol{E}^{\text{sc}} \cdot \boldsymbol{\tau}_2 = -\boldsymbol{E}^{\text{imp}} \cdot \boldsymbol{\tau}_2$. Hence, the boundary condition (7b) alone still leaves the problem underdetermined. It is the additional boundary condition for divergence (7c) that provides the missing third scalar relation at the boundary and thus enables well-posedness of the overall formulation (7). Equation (7c) is a Neumann-type boundary condition because it involves a normal derivative of the normal field component (see Section 5 for implementation detail).

Let us also re-emphasize that in the Cartesian coordinates, the vector wave equation (7a) decouples into three scalar wave equations. However, the boundary conditions (7b)–(7c) still enforce coupling at the boundary $\partial\Omega$ between all three Cartesian components of the electric field.

Hereafter, we will be using a simpler "plain" notation $\boldsymbol{E}$ instead of $\boldsymbol{E}^{\text{sc}}$ for the scattered field on $\mathbb{R}^3\backslash\Omega$, as long as it does not lead to any misunderstanding.

1.4. Solving Maxwell's equations in first-order form vs. second-order form

Maxwell's equations are often solved in their original first-order form (1). A popular family of numerical methods, known as finite-difference time-domain methods (FDTD) [8], originate from the second-order accurate staggered Yee scheme [9] proposed in 1966. Other methods such as spectral can be applied as well, see, e.g., [10]. Various material properties can be accommodated, for example, dispersion [11,12].

However, the second-order form of Maxwell's equations (3) has its own advantages. A number of publications study numerical solution of Maxwell's equations in second-order form [13–17], including the scenarios with material dispersion [18–21]. Otherwise, the advantages of solving the second-order wave equations rather than their first-order counterparts are discussed in [22,23] for acoustics, [24] for elasticity, and [25] for a general framework.

First and foremost, the second-order formulation enables decoupling of Maxwell's equations, as described in Sections 1.2 and 1.3. Decoupling takes place only in the volume while the fields and/or their components remain coupled at the boundary. Decoupling is not a model reduction and the new second-order formulation is equivalent to the original first-order one. Yet it presents a major simplification from the standpoint of numerical solution. The scenario where one can solve for one field without having to solve for the other is especially favorable. But even when solving for both fields, the capacity to time-march them independently and only enforce the coupling at the boundary is convenient. Decoupling between the individual Cartesian components of the fields is also convenient as it lets one exploit the existing wealth of schemes and solvers for the scalar wave equation. In particular, the solvers based on Calderon's operators and the method of difference potentials (MDP) [26] that we have developed previously [1–3] and are using in this paper, offer an extra advantage for the treatment of the boundary conditions. Namely, the MDP reduces the governing PDEs from the domain to the boundary regardless of any boundary conditions. Therefore, the coupling between the field components at the boundary is easy to address by merely adding the boundary conditions (7b)–(7c) to the corresponding system of Calderon's boundary equations that is otherwise derived from the three independent wave equations.

Another key advantage of the second order formulation is that, compact high-order accurate schemes for the scalar wave equation are relatively easy to derive, see, e.g., [27] or [28]. Both compactness and high-order accuracy are valuable properties. High-order accuracy is of central importance for reducing the numerical pollution [29,30]. Compactness substantially simplifies the discretization because compact schemes require only as many boundary conditions as the underlying PDE does. On the other hand, extension of the classical staggered Yee scheme [9] to high-order accuracy is not straightforward. Most high-order accurate FDTD schemes are not compact. They rely on wide stencils which, in turn, require additional (non-physical) boundary conditions. Even if a staggered high-order accurate compact discretization is built for Maxwell's equations (1), see, e.g., [31], it still requires a rather delicate analysis near the boundary, because different field components are associated with different locations in space. The difference in spatial location for different field components is what may, in general, cause difficulties in implementing the boundary conditions with staggered schemes, for example, the impedance boundary condition (5). Let's also note that, high-order accurate schemes for first-order Maxwell's equations can be constructed by exploiting some approaches, such as WENO, developed for CFD, see, e.g., [32]. The resulting techniques prove viable even though Maxwell's equations are not conservation laws.

1.5. Roadmap

In the rest of the paper, we present our new high-order accurate numerical algorithm for solving the second-order initial boundary value problem (IBVP) (7). The main novel contributions of the current work are the accurate formulation of the IBVP (7) per se, the approach for taking into account the vector nature of the unknown field $\boldsymbol{E}$ for numerical solution (three Cartesian components), as well as the technique for implementing the boundary conditions (7b) and (7c). Other components of the proposed algorithm are similar to what we have developed previously for the scalar setting (acoustics), see [1–3].

In Section 2, we show how to define the scattering surface using CAD and introduce a piece-wise parameterization of this surface by means of high-oder splines. In Section 3, we provide a brief description of the method of difference potentials for unsteady problems and show how to apply it in conjunction with the (strong) Huygens' principle, which enables a non-deteriorating performance over arbitrarily long simulation times and guarantees a perfectly non-reflecting treatment of the artificial outer boundary. In Section 4, we extend the apparatus of difference potentials from the previously analyzed scalar case to the case of the vector wave equation (7a). In Section 5, we introduce a new collocation method for taking into account the boundary conditions (7b) and (7c). In Section 6, we demonstrate the performance of the proposed method by computing the electromagnetic scattering about a PEC sphere (Section 6.1) and about a PEC double-cone hypersonic shape (Section 6.2). Finally in Section 7, we conclude that the proposed method meets its design characteristics and also summarize the possible directions of the future work.

2. Definition of the scattering surface

The scattering surface $\partial\Omega$ is a two-dimensional manifold in $\mathbb{R}^3$. It is therefore convenient to represent it parametrically by means of a mapping from $\mathbb{R}^2$ to $\mathbb{R}^3$. If, for example, $\partial\Omega$ is a sphere of radius r, then one can use the standard spherical coordinates transformation:

$$x = r\sin\theta\cos\varphi, \quad y = r\sin\theta\sin\varphi, \quad z = r\cos\theta \tag{8}$$

from the rectangle $[0,\pi]\times[0,2\pi) \ni (\theta,\varphi)$ to the sphere, where θ is the polar angle and φ is the azimuthal angle. However, only a small number of relatively simple surfaces (such as spheroids or toroids) can be parameterized by means of one and the same coordinate transformation [33, Volume 1]. For all other surfaces, one can use a patched parametrization.

Let $\partial\Omega = P_1 \cup P_2 \cup \ldots \cup P_{N_p}$, where $P_j \cap P_i = \emptyset$ for $j \neq i$. For each $j = 1,2,\ldots,N_p$, the patch P_j is defined by means of a differentiable mapping $\hat{\boldsymbol{X}}_j : \hat{P}_j \mapsto P_j$:

$$\mathbb{R}^3 \supset P_j \ni \boldsymbol{x} = \hat{\boldsymbol{X}}_j(s_1,s_2), \quad \text{where} \quad (s_1,s_2) \in \hat{P}_j \subset \mathbb{R}^2. \tag{9}$$

In formula (9), $\hat{P}_j$ is a 2D reference domain and (s_1,s_2) are the parametric coordinates. In the case of a sphere, we have $N_p = 1$ and the mapping $\hat{\boldsymbol{X}}_1$ of (9) would be given by the spherical coordinate transformation (8) so that $s_1 = \theta$, $s_2 = \varphi$, and $\hat{P}_1 = [0,\pi]\times[0,2\pi)$.

In the general case where the surface is represented using CAD, it is common to define the mapping (9) with the help of splines. In particular, for each $j = 1,2,\ldots,N_p$, one can employ the non-uniform rational B-splines (NURBS) [34] as functions of the parametric coordinates:

$$\hat{\boldsymbol{X}}_j(s_1,s_2) = \sum_{i_1=1}^{n_1}\sum_{i_2=1}^{n_2} \boldsymbol{x}_{i_1,i_2} N^{(i_1,d_1)}(s_1) N^{(i_2,d_2)}(s_2). \tag{10}$$

In formula (10), $\boldsymbol{x}_{i_1,i_2} \in \mathbb{R}^3$ are the control points and $N^{(i_1,d_1)}(s_1)$ and $N^{(i_2,d_2)}(s_2)$ are NURBS of degree d_1 and d_2, respectively. The NURBS are defined as follows.

First, for a given coordinate s, consider a sequence of knots $\{k_1,k_2,\ldots,k_{n+d+1}\}$, where the positive integers n and d are given, $n > d$, and the first and last knots are repeated $d+1$ times each: $k_1 = k_2 = \ldots = k_{d+1}$ and $k_{n+1} = k_{n+2} = \ldots = k_{n+d+1}$. Then, introduce the "plain" B-splines of degree d using the Cox–de Boor recursion:

$$B^{(i,0)}(s) = \begin{cases} 1, & k_i \leqslant s < k_{i+1}, \\ 0, & \text{otherwise} \end{cases}$$

and

$$B^{(i,d)}(s) = \frac{s-k_i}{k_{i+d}-k_i} B^{(i,d-1)}(s) + \frac{k_{i+d+1}-s}{k_{i+d+1}-k_{i+1}} B^{(i+1,d-1)}(s).$$

Finally, specify the weights $\{w_1,w_2,\ldots,w_n\}$ and define a 1D NURBS:

$$N^{(i,d)}(s) = \frac{w_i B^{(i,d)}(s)}{\sum_{j=1}^{n} w_j B^{(j,d)}(s)}. \tag{11}$$

If $w_1 = w_2 = \ldots = w_n = 1$, then $N^{(i,d)}(s) = B^{(i,d)}(s)$. In formula (10), both $N^{(i_1,d_1)}(s_1)$ and $N^{(i_2,d_2)}(s_2)$ are defined according to (11), but the degrees d_1 and d_2, dimensions n_1 and n_2, as well as the knots and weights for s_1 and s_2, can be different.

3. Calderon's operators, difference potentials, and Huygens' principle

In this section, we provide a brief account of the MDP for unsteady problems and refer the reader to [1–3] for further detail.

3.1. Calderon's operators for the scalar wave equation

The scattered field $\boldsymbol{E} = (E_x,E_y,E_z)$ satisfies the vector wave equation (7a). Accordingly, its Cartesian components satisfy the scalar wave (d'Alembert) equation:

$$\Box_c E \equiv \frac{1}{c^2}\frac{\partial^2 E}{\partial t^2} - \Delta E = 0, \tag{12}$$

where E can be any of E_x, E_y, or E_z. Let $\Gamma_t = \partial\Omega\times[0,t]$, where $t \leqslant T$ is the current moment of time. Let $\boldsymbol{\xi}_{\Gamma_t}$ denote a two-dimensional vector function on Γ_t, $\boldsymbol{\xi}_{\Gamma_t} = (\xi_0,\xi_1)$. Also, for an arbitrary $E = E(\boldsymbol{x},t)$, define its vector trace on Γ_t: $\boldsymbol{Tr}_{\Gamma_t} E \overset{\text{def}}{=} \left(E, \frac{\partial E}{\partial \boldsymbol{n}}\right)\Big|_{\Gamma_t}$.

The function $E = E(\boldsymbol{x},t)$ solves the wave equation (12) on $\Omega_1 \equiv \mathbb{R}^3 \setminus \Omega$ subject to homogeneous initial conditions, cf. (7d), if and only if its trace $\boldsymbol{\xi}_{\Gamma_t} = \boldsymbol{Tr}_{\Gamma_t} E$ satisfies the Calderon's boundary equation with projection (BEP):

$$\boldsymbol{P}_{\Gamma_t}\boldsymbol{\xi}_{\Gamma_t} = \boldsymbol{\xi}_{\Gamma_t}. \tag{13}$$

The projection P_{Γ_t} in (13) is defined via Calderon's potential with density ξ_{Γ_t}:

$$P_{\Omega_1}\xi_{\Gamma_t}(x,t) = \int\limits_{\Gamma_t} \left\{ \xi_1(y,t')G(x-y,t-t') - \xi_0(y,t')\frac{\partial G}{\partial n}(x-y,t-t') \right\} dt'dS_y \tag{14}$$

as its trace on Γ_t:

$$P_{\Gamma_t}\xi_{\Gamma_t} \overset{\text{def}}{=} Tr_{\Gamma_t} P_{\Omega_1}\xi_{\Gamma_t}.$$

In formula (14), $G(x,t) = \frac{c}{2\pi}\theta(t)\delta(c^2t^2 - |x|^2)$ is the fundamental solution of the 3D d'Alembert operator $\Box_c$ of (12). For any ξ_{Γ_t}, the potential (14) with density ξ_{Γ_t} satisfies the wave equation (12) on Ω_1. If, on the other hand, ξ_{Γ_t} is the trace of a solution E to equation (12) on Ω_1, then (14) becomes the classical Green's formula.

3.2. Partition in time

Let K be a positive integer and $T_0 = T/K$. Split Γ_T into K equal parts of length T_0:

$$\Gamma_T = \Gamma^{(1)} \cup \Gamma^{(2)} \cup \ldots \cup \Gamma^{(K)}, \quad \text{where} \quad \Gamma^{(k)} = \partial\Omega \times ((k-1)T_0, kT_0], \tag{15}$$

and represent ξ_{Γ_T} as the sum of partial densities:

$$\xi_{\Gamma_T} = \xi_{\Gamma^{(1)}} + \xi_{\Gamma^{(2)}} + \ldots + \xi_{\Gamma^{(K)}}, \text{ where } \xi_{\Gamma^{(k)}}(x,t) = \begin{cases} \xi_{\Gamma_T}(x,t), & (x,t) \in \Gamma^{(k)}, \\ 0, & (x,t) \in \Gamma_T \backslash \Gamma^{(k)}. \end{cases}$$

Then, using the definitions of the operators (Section 3.1) and taking into account the causality, we can recast the BEP (13) for $t = T$: $P_{\Gamma_T}\xi_{\Gamma_T} = \xi_{\Gamma_T}$, as a recursive sequence:

$$Tr_{\Gamma^{(k)}} P_{\Omega_1}\xi_{\Gamma^{(k)}} + {\sum_{j=1}^{k-1}}' Tr_{\Gamma^{(k)}} P_{\Omega_1}\xi_{\Gamma^{(j)}} = \xi_{\Gamma^{(k)}}, \quad k = 1, \ldots, K. \tag{16}$$

For $k = 1$, the second term on the left-hand side of equation (16), i.e., the primed sum from $j = 1$ to $k-1$, is dropped. For the first term on the left-hand side of (16), we can write:

$$\begin{aligned} P_{\Omega_1}\xi_{\Gamma^{(k)}}(x,t) &= \int\limits_{\Gamma^{(k)}} \left\{ \xi_1(y,t')G(x-y,t-t') - \xi_0(y,t')\frac{\partial G}{\partial n}(x-y,t-t') \right\} dt'dS_y \\ &= \int\limits_{\Gamma_{T_0}} \Big\{ \xi_1(y,\tilde{t}' + (k-1)T_0)G(x-y,\tilde{t}-\tilde{t}') \\ &\qquad - \xi_0(y,\tilde{t}' + (k-1)T_0)\frac{\partial G}{\partial n}(x-y,\tilde{t}-\tilde{t}') \Big\} d\tilde{t}'dS_y, \end{aligned} \tag{17}$$

where $t = \tilde{t} + (k-1)T_0$ and $0 \leqslant \tilde{t} \leqslant T_0$. Also, $\Gamma_{T_0} \equiv \Gamma^{(1)}$. Therefore, equation (16) becomes:

$$P_{\Gamma_{T_0}}\xi_{\Gamma^{(k)}} + {\sum_{j=1}^{k-1}}' Tr_{\Gamma^{(k)}} P_{\Omega_1}\xi_{\Gamma^{(j)}} = \xi_{\Gamma^{(k)}}, \quad k = 1, \ldots, K, \tag{18}$$

where the operator $P_{\Gamma_{T_0}} = P_{\Gamma_t}\big|_{t=T_0}$ does not depend on k. As in equation (16), the primed sum on the left-hand side of equation (18) is dropped for $k = 1$. The first term on the left-hand side of (18) is a shorthand notation for the function on $\Gamma^{(k)}$ defined in accordance with (17):

$$\begin{aligned} P_{\Gamma_{T_0}}\xi_{\Gamma^{(k)}} &\overset{\text{def}}{=} \left[P_{\Gamma_{T_0}}\xi_{\Gamma^{(k)}}(\tilde{t} + (k-1)T_0)\right](t - (k-1)T_0), \\ &(k-1)T_0 < t \leqslant kT_0, \quad 0 \leqslant \tilde{t} \leqslant T_0. \end{aligned} \tag{19}$$

Equation (18) is a recursion with respect to k. It shows that the partial density $\xi_{\Gamma^{(k)}}$ depends on all previous partial densities $\xi_{\Gamma^{(j)}}$, $j = k-1, k-2, \ldots, 1$. As, however, will be shown in the next section, the dependence of $\xi_{\Gamma^{(k)}}$ on $\xi_{\Gamma^{(j)}}$, $j < k-1$, can be truncated because the wave equation (12) satisfies the strong Huygens' principle.

3.3. Huygens' principle

Consider equation (18), which holds on $\Gamma^{(k)}$. For each j on its left-hand side, we can write (cf. the first line of equation (17)):

$$P_{\Omega_1}\xi_{\Gamma^{(j)}}(x,t)=\int\limits_{\Gamma^{(j)}}\left\{\xi_1(y,t')G(x-y,t-t')-\xi_0(y,t')\frac{\partial G}{\partial n}(x-y,t-t')\right\}dt'dS_y. \tag{20}$$

Since $(x,t)\in\Gamma^{(k)}$ and the support of the fundamental solution G under the integral in (20) is the surface of the characteristic cone with the vertex (x,t), the integral may be non-zero only if this surface intersects with $\Gamma^{(j)}$. In turn, the intersection may be non-empty only if

$$jT_0>t-\frac{1}{c}\operatorname{diam}\Omega.$$

For $(x,t)\in\Gamma^{(k)}$ in (20), we have $t>(k-1)T_0$. Then, from the previous inequality, we derive:

$$(k-1-j)T_0<\frac{1}{c}\operatorname{diam}\Omega. \tag{21}$$

Next, let us choose T_0 in accordance with

$$T_0\geqslant\frac{1}{c}\operatorname{diam}\Omega. \tag{22}$$

In this case, the inequality (21) holds only for $j=k-1$ and does not hold for any $j<k-1$. Consequently, only one non-zero term remains in the sum on the left-hand side of (18):

$$\begin{aligned}&P_{\Gamma_{T_0}}\xi_{\Gamma^{(1)}}=\xi_{\Gamma^{(1)}},\quad k=1,\\ &P_{\Gamma_{T_0}}\xi_{\Gamma^{(k)}}+Tr_{\Gamma^{(k)}}P_{\Omega_1}\xi_{\Gamma^{(k-1)}}=\xi_{\Gamma^{(k)}},\quad k=2,\dots,K.\end{aligned} \tag{23}$$

The fact that the fundamental solution G of the three-dimensional d'Alembert operator differs from zero only on the surface of the characteristic cone is a manifestation of the strong Huygens' principle. The interior of the cone is known as lacuna of the fundamental solution. It is therefore the Hugens' principle that allows one to truncate the recursion (18) and replace it with equations (23). The latter indicate that under the assumption (22), the partial density $\xi_{\Gamma^{(k)}}$ depends only on one immediately preceding density $\xi_{\Gamma^{(k-1)}}$.

Similarly to (17), we can derive from (20) for $j=k-1$:

$$\begin{aligned}P_{\Omega_1}\xi_{\Gamma^{(k-1)}}(x,t)=\int\limits_{\Gamma_{T_0}}\Big\{&\xi_1(y,\tilde{t}'+(k-2)T_0)G(x-y,\tilde{t}-\tilde{t}')\\ &-\xi_0(y,\tilde{t}'+(k-2)T_0)\frac{\partial G}{\partial n}(x-y,\tilde{t}-\tilde{t}')\Big\}d\tilde{t}'dS_y,\end{aligned}$$

where $t=\tilde{t}+(k-2)T_0$ and $T_0\leqslant\tilde{t}\leqslant 2T_0$. Then, we introduce another shorthand notation:

$$\begin{aligned}R_{\Gamma_{T_0}}\xi_{\Gamma^{(k-1)}}\overset{\text{def}}{=}&\left[Tr_{\Gamma^{(2)}}P_{\Omega_1}\xi_{\Gamma^{(k-1)}}(\tilde{\tilde{t}}+(k-2)T_0)\right](t-(k-2)T_0),\\ &(k-1)T_0<t\leqslant kT_0,\quad 0\leqslant\tilde{\tilde{t}}\leqslant T_0,\end{aligned} \tag{24}$$

so that similar to $P_{\Gamma_{T_0}}$ of (19), the operator $R_{\Gamma_{T_0}}$ of (24) does not depend on k. The operator $R_{\Gamma_{T_0}}$ maps a given $\xi_{\Gamma^{(k-1)}}$ to a density defined on the next partition element $\Gamma^{(k)}$. Accordingly, equations (23) are recast as

$$\begin{aligned}&P_{\Gamma_{T_0}}\xi_{\Gamma^{(1)}}=\xi_{\Gamma^{(1)}},\quad k=1,\\ &P_{\Gamma_{T_0}}\xi_{\Gamma^{(k)}}+R_{\Gamma_{T_0}}\xi_{\Gamma^{(k-1)}}=\xi_{\Gamma^{(k)}},\quad k=2,\dots,K.\end{aligned} \tag{25}$$

Equations (25) can be interpreted as time marching along the boundary Γ_T with step size T_0.

Equations (25) on their own are not sufficient for determining $\xi_{\Gamma^{(k)}}$, $k=1,\dots,K$, because they need to be supplemented with the boundary conditions. We will discuss the boundary conditions in Section 5, after we have discretized equations (25) using difference potentials (Section 3.4) and extended them to the vector framework (Section 4).

3.4. Difference potentials and projections

The discretization of equations (25) by difference potentials [26] consists of three steps: the discretization of the densities $\xi_{\Gamma^{(k)}}$ and $\xi_{\Gamma^{(k-1)}}$ on the surface $\partial\Omega$, the discretization of the operators $P_{\Gamma_{T_0}}$ and $R_{\Gamma_{T_0}}$ on a volumetric grid near $\partial\Omega$, and the combination of the two that allows one to solve the resulting discrete equations with respect to the unknowns on the surface while having the operators computed conveniently on a regular grid in the volume.

For the densities $\boldsymbol{\xi}_{\Gamma^{(k)}}$ and $\boldsymbol{\xi}_{\Gamma^{(k-1)}}$, we use a spectral discretization. All partial boundaries (15) are geometrically identical, they are merely shifted in time with respect to one another. Hence, we can introduce the same basis functions ψ_m, $m = 1, \dots, M$, for all $\Gamma^{(k)}$, $k = 1, \dots, K$. Recall that, the scattering surface $\partial\Omega$ is composed of N_p patches (Section 2). The basis functions ψ_m are chosen independently for every patch P_j, $j = 1, \dots, N_p$, as functions of three variables: the parametric coordinates $(s_1, s_2) \in \hat{P}_j$ (see formulae (9)–(10)) and time $t \in [0, T_0]$. For convenience, we consider all ψ_m defined on the entire $\partial\Omega$ and enumerate them consecutively throughout. However, each ψ_m is non-zero only on one patch and zero on all others. On this one patch, it is taken as a combination of Fourier harmonics and Chebyshev polynomials (see Section 6). If there are M_j basis functions that correspond to the patch P_j (i.e., they are non-zero on this patch), then the total number of basis functions is $M = \sum_{j=1}^{N_p} M_j$. The choice of the dimensions M_j is discussed in Section 6.

As $\boldsymbol{\xi}_{\Gamma^{(k)}}$ and $\boldsymbol{\xi}_{\Gamma^{(k-1)}}$ are vector functions, we expand them with respect to $\boldsymbol{\psi}_{0,m} = (\psi_m, 0)$ and $\boldsymbol{\psi}_{1,m} = (0, \psi_m)$:

$$\boldsymbol{\xi}_{\Gamma^{(k)}} = \sum_{m=1}^{M} c_{0,m}^{(k)} \boldsymbol{\psi}_{0,m} + c_{1,m}^{(k)} \boldsymbol{\psi}_{1,m}, \quad \boldsymbol{\xi}_{\Gamma^{(k-1)}} = \sum_{m=1}^{M} c_{0,m}^{(k-1)} \boldsymbol{\psi}_{0,m} + c_{1,m}^{(k-1)} \boldsymbol{\psi}_{1,m}. \tag{26}$$

Substituting (26) into (25), we obtain:

$$\sum_{m=1}^{M} c_{0,m}^{(1)} \boldsymbol{Q}_{\Gamma_{T_0}} \boldsymbol{\psi}_{0,m} + c_{1,m}^{(1)} \boldsymbol{Q}_{\Gamma_{T_0}} \boldsymbol{\psi}_{1,m} = 0, \quad k = 1, \tag{27a}$$

and

$$\sum_{m=1}^{M} c_{0,m}^{(k)} \boldsymbol{Q}_{\Gamma_{T_0}} \boldsymbol{\psi}_{0,m} + c_{1,m}^{(k)} \boldsymbol{Q}_{\Gamma_{T_0}} \boldsymbol{\psi}_{1,m} = -\sum_{m=1}^{M} c_{0,m}^{(k-1)} \boldsymbol{R}_{\Gamma_{T_0}} \boldsymbol{\psi}_{0,m} + c_{1,m}^{(k-1)} \boldsymbol{R}_{\Gamma_{T_0}} \boldsymbol{\psi}_{1,m}, \tag{27b}$$
$$k = 2, \dots, K,$$

where $\boldsymbol{Q}_{\Gamma_{T_0}} \overset{\text{def}}{=} \boldsymbol{P}_{\Gamma_{T_0}} - \boldsymbol{I}$, and $\boldsymbol{I}$ is the identity operator. The operators $\boldsymbol{Q}_{\Gamma_{T_0}}$ and $\boldsymbol{R}_{\Gamma_{T_0}}$ in (27) do not depend on k and neither do the basis functions $\boldsymbol{\psi}_{0,m}$ and $\boldsymbol{\psi}_{1,m}$. As such, the boundary vector functions $\boldsymbol{Q}_{\Gamma_{T_0}} \boldsymbol{\psi}_{0,m}$, $\boldsymbol{Q}_{\Gamma_{T_0}} \boldsymbol{\psi}_{1,m}$, $\boldsymbol{R}_{\Gamma_{T_0}} \boldsymbol{\psi}_{0,m}$, and $\boldsymbol{R}_{\Gamma_{T_0}} \boldsymbol{\psi}_{1,m}$ are also k-independent. Hence, equations (27) can be thought of as a plain recursion with respect to $k = 1, 2, \dots, K$ for the expansion coefficients $c_{0,m}^{(k)}$ and $c_{1,m}^{(k)}$, $m = 1, \dots, M$. Specifically, for $k = 1$ we have equation (27a), which is a homogeneous equation for the unknown coefficients $c_{0,m}^{(1)}$ and $c_{1,m}^{(1)}$. For all subsequent $k = 2, \dots, K$, we have equation (27b), which is an inhomogeneous equation for the unknown coefficients $c_{0,m}^{(k)}$ and $c_{1,m}^{(k)}$, whereas the coefficients $c_{0,m}^{(k-1)}$ and $c_{1,m}^{(k-1)}$ determined on the previous step can be considered known.

Equations (27) still need to be supplemented with the boundary conditions to enable a unique solution (see Section 5). Prior to that, equations (27) shall be fully discretized because as of yet, the operators $\boldsymbol{Q}_{\Gamma_{T_0}}$ and $\boldsymbol{R}_{\Gamma_{T_0}}$ still remain continuous.

To discretize $\boldsymbol{Q}_{\Gamma_{T_0}}$ and $\boldsymbol{R}_{\Gamma_{T_0}}$, we first replace the definition (14) of Calderon's potential $\boldsymbol{P}_{\Omega_1} \boldsymbol{\xi}_{\Gamma_t}$ with an equivalent definition that involves no boundary integrals. For a given $\boldsymbol{\xi}_{\Gamma_t}$, consider the initial-value problem that we will call the auxiliary problem (AP):

$$\begin{gathered} \frac{1}{c^2} \frac{\partial^2 v}{\partial t^2} - \Delta v = \begin{cases} \Box_c w, & \boldsymbol{x} \in \Omega, \\ 0, & \boldsymbol{x} \in \Omega_1, \end{cases} \\ v\Big|_{t=0} = \begin{cases} w\Big|_{t=0}, & \boldsymbol{x} \in \Omega, \\ 0, & \boldsymbol{x} \in \Omega_1, \end{cases} \qquad \frac{\partial v}{\partial t}\Big|_{t=0} = \begin{cases} \frac{\partial w}{\partial t}\Big|_{t=0}, & \boldsymbol{x} \in \Omega, \\ 0, & \boldsymbol{x} \in \Omega_1. \end{cases} \end{gathered} \tag{28}$$

In formula (28), $w = w(\boldsymbol{x}, t)$ can be any sufficiently smooth function such that $\boldsymbol{Tr}_{\Gamma_t} w = \boldsymbol{\xi}_{\Gamma_t}$. Then, on the domain $\Omega_1 = \mathbb{R}^3 \setminus \Omega$, the solution $v = v(\boldsymbol{x}, t)$ of the AP (28) coincides with Calderon's potential (14):

$$v(\boldsymbol{x}, t) = \boldsymbol{P}_{\Omega_1} \boldsymbol{\xi}_{\Gamma_t}(\boldsymbol{x}, t), \quad \boldsymbol{x} \in \Omega_1.$$

Consequently, to compute $\boldsymbol{P}_{\Gamma_{T_0}} \boldsymbol{\xi}_{\Gamma_{T_0}}$ for a given $\boldsymbol{\xi}_{\Gamma_{T_0}}$, see formula (19), it will be sufficient solve the AP (28) on the interval $t \in [0, T_0]$. Likewise, to compute $\boldsymbol{R}_{\Gamma_{T_0}} \boldsymbol{\xi}_{\Gamma_{T_0}}$ for a given $\boldsymbol{\xi}_{\Gamma_{T_0}}$, see formula (24), one should solve the AP (28) on the interval $t \in [0, 2T_0]$.

The AP (28) is solved by finite differences. Any appropriate scheme can be used that would be sufficiently accurate and easy/inexpensive to implement. The grid can be simple, e.g., Cartesian, while the boundary $\partial\Omega$ can be non-conforming. For the simulations in Section 6, we use non-staggered schemes (Section 1.4), where the solution variables and residuals of the difference equations are attributed to the same nodes.

Moreover, since the AP does not need to be solved beyond $t = 2T_0$, it requires no artificial boundary conditions (ABCs) [35–37]. The artificial outer boundary can merely be placed sufficiently far away from the compactly supported sources inside Ω so that by the time the computation is terminated ($t = 2T_0$), no reflections can reach Ω yet. In this sense, the partition (15) along with Huygens' principle facilitate the exact treatment of the artificial outer boundary. The reflections do not affect the solution because they are not present in the region of interest rather than because they are suppressed or minimized in any particular way. We have exploited

this approach in the case of acoustics (scalar) [3]. In the current work, it applies to the case of electromagnetism (vector) with no modifications.

Let $\mathbb{N}^0$ be the spatial discretization grid for the AP (28). This grid extends at least $2T_0/c$ away from Ω in every direction so that no ABCs are required. Let $\mathbb{N}^+ = \mathbb{N}^0 \cap \Omega$ and $\mathbb{N}^- = \mathbb{N}^0 \setminus \mathbb{N}^+ = \mathbb{N}^0 \cap \Omega_1$. Let t be the current (discrete) moment of time and $\mathbb{N}^0_t$, $\mathbb{N}^+_t$ and $\mathbb{N}^-_t$ be the corresponding space-time grids. The spatial "snapshots" of those grids are the same on every time level because the shape of Ω is fixed. Let $\mathbb{S}_{\mathfrak{n}}$ be the stencil of the discretization scheme centered at the node $\mathfrak{n}$ of the grid $\mathbb{N}^0_t$. The grid boundary is defined as follows:

$$\gamma_t = \left\{ \bigcup_{\mathfrak{n}\in\mathbb{N}^+_t} \mathbb{S}_{\mathfrak{n}} \right\} \bigcap \left\{ \bigcup_{\mathfrak{n}\in\mathbb{N}^-_t} \mathbb{S}_{\mathfrak{n}} \right\}. \tag{29}$$

It is a multi-layer fringe of grid nodes that straddles the continuous boundary Γ_t. Assume (with no loss of generality) that the stencil $\mathbb{S}_{\mathfrak{n}}$ is also fixed. Then, the grid boundary γ_t of (29) is the same on every time level. We will denote by γ the spatial projection of γ_t.

Let the discrete density ξ_{γ_t} be given. It is a plain grid function defined on γ_t of (29). Let the auxiliary grid function $w^{(h)}$ be equal to ξ_{γ_t} on γ_t and 0 on $\mathbb{N}^0_t \setminus \gamma_t$. With $w^{(h)}$ available, the AP (28) is discretized on the grid $\mathbb{N}^0_t$:

$$\begin{aligned} &\Box^{(h)}_c v^{(h)} = \begin{cases} \Box^{(h)}_c w^{(h)}, & \mathfrak{n} \in \mathbb{N}^+_t, \\ 0, & \mathfrak{n} \in \mathbb{N}^-_t, \end{cases} \\ &v^{(h)} = w^{(h)}, \quad \mathfrak{n} \in \text{two initial time levels on } \mathbb{N}^+. \end{aligned} \tag{30}$$

The difference Calderon's projection is the trace of the solution $v^{(h)}$ to the discrete AP (30):

$$\boldsymbol{P}_{\gamma_t}\xi_{\gamma_t} \overset{\text{def}}{=} v^{(h)}\Big|_{\gamma_t}. \tag{31}$$

A grid function $E^{(h)}$ satisfies the discrete wave equation $\Box^{(h)}_c E^{(h)} = 0$ on $\mathbb{N}^-_t$ subject to homogeneous initial conditions if and only if its trace $\xi_{\gamma_t} = E^{(h)}\Big|_{\gamma_t}$ satisfies the difference Calderon's boundary equation with projection [cf. equation (13)]:

$$\boldsymbol{P}_{\gamma_t}\xi_{\gamma_t} = \xi_{\gamma_t}. \tag{32}$$

The discrete operators $\boldsymbol{Q}_{\gamma_{T_0}} = \boldsymbol{P}_{\gamma_{T_0}} - \boldsymbol{I}$ and $\boldsymbol{R}_{\gamma_{T_0}}$ are defined similar to $\boldsymbol{Q}_{\Gamma_{T_0}}$ and $\boldsymbol{R}_{\Gamma_{T_0}}$, respectively (see formulae (19) and (24)). The main difference is that the surface potentials are replaced with the corresponding solutions of the difference AP (30).

In addition to the operators $\boldsymbol{Q}_{\gamma_{T_0}}$ and $\boldsymbol{R}_{\gamma_{T_0}}$, we will need to introduce the extension operator $\boldsymbol{Ex}$ that maps a given continuous density $\boldsymbol{\xi}_{\Gamma_t}$ onto a discrete density ξ_{γ_t}:

$$\xi_{\gamma_t} = \boldsymbol{Ex}\boldsymbol{\xi}_{\Gamma_t}. \tag{33}$$

Let $\mathfrak{n} \in \gamma$ be a grid node near the boundary $\partial\Omega$, and let $\bar{\mathfrak{n}} \in \partial\Omega$ be the closest point to $\mathfrak{n}$ on the surface (foot of the normal dropped from $\mathfrak{n}$ onto $\partial\Omega$). At $\bar{\mathfrak{n}}$, we have the function and its first normal derivative available: $(\xi_0, \xi_1) = \left(E, \frac{\partial E}{\partial n}\right)$. To obtain higher-order normal derivatives, we recast the governing d'Alembert equation (12) in local surface-oriented coordinates [38] defined as follows. If $\bar{\mathfrak{n}} \in P_j$, then the location of the node $\mathfrak{n}$ is uniquely characterized by three real numbers: $(s_1, s_2) \in \hat{P}_j$ (see formulae (9)–(10)) and the distance z' between $\mathfrak{n}$ and $\bar{\mathfrak{n}}$, which is positive if $\mathfrak{n} \in \Omega_1$ (outside $\partial\Omega$) and negative if $\mathfrak{n} \in \Omega$ (inside $\partial\Omega$). The same characterization (two parametric coordinates on the surface and a signed distance z' along the normal) applies to every point in $\mathbb{R}^3$ sufficiently close to $\partial\Omega$. In surface-oriented coordinates (s_1, s_2, z'), the second-order normal derivative is obtained directly from the wave equation via the tangential derivatives, first-order normal derivative, and second-order time derivative, while higher order normal derivatives are obtained by differentiating equation (12). With sufficiently many normal derivatives at hand, the value of ξ_{γ_t} at $\mathfrak{n}$ is reconstructed by Taylor's formula. The order of the Taylor's formula is related to the desired accuracy of approximation. If the scheme (30) is second-order accurate, it is sufficient to use the Taylor's formula up to the second derivative. For a fourth-order accurate scheme, one should include the terms up to the fourth derivative. Further details can be found in [3, Section 4].

Having introduced the AP (28) and its discretization (30), and having constructed the difference BEP (32) and extension operator (33), we can obtain a discrete counterpart to (27):

$$\sum_{m=1}^{M} c^{(1)}_{0,m} \boldsymbol{Q}_{\gamma_{T_0}} \boldsymbol{Ex}\boldsymbol{\psi}_{0,m} + c^{(1)}_{1,m} \boldsymbol{Q}_{\gamma_{T_0}} \boldsymbol{Ex}\boldsymbol{\psi}_{1,m} = 0, \quad k = 1, \tag{34a}$$

$$\begin{aligned} &\sum_{m=1}^{M} c^{(k)}_{0,m} \boldsymbol{Q}_{\gamma_{T_0}} \boldsymbol{Ex}\boldsymbol{\psi}_{0,m} + c^{(k)}_{1,m} \boldsymbol{Q}_{\gamma_{T_0}} \boldsymbol{Ex}\boldsymbol{\psi}_{1,m} = \\ &\qquad - \sum_{m=1}^{M} c^{(k-1)}_{0,m} \boldsymbol{R}_{\gamma_{T_0}} \boldsymbol{Ex}\boldsymbol{\psi}_{0,m} + c^{(k-1)}_{1,m} \boldsymbol{R}_{\gamma_{T_0}} \boldsymbol{Ex}\boldsymbol{\psi}_{1,m}, \quad k = 2, \ldots, K. \end{aligned} \tag{34b}$$

Equations (34) are convenient to recast in matrix notation:

$$\boldsymbol{Q}^{(0)}_{\gamma_{T_0}} \boldsymbol{c}^{(1)}_0 + \boldsymbol{Q}^{(1)}_{\gamma_{T_0}} \boldsymbol{c}^{(1)}_1 = \boldsymbol{0}, \quad k = 1, \tag{35a}$$

$$\boldsymbol{Q}^{(0)}_{\gamma_{T_0}} \boldsymbol{c}^{(k)}_0 + \boldsymbol{Q}^{(1)}_{\gamma_{T_0}} \boldsymbol{c}^{(k)}_1 = -\boldsymbol{R}^{(0)}_{\gamma_{T_0}} \boldsymbol{c}^{(k-1)}_0 - \boldsymbol{R}^{(1)}_{\gamma_{T_0}} \boldsymbol{c}^{(k-1)}_1, \quad k = 2, \dots, K, \tag{35b}$$

where

$$\boldsymbol{c}^{(k)}_0 = [c^{(k)}_{0,1}, c^{(k)}_{0,2}, \dots, c^{(k)}_{0,M}]^T, \quad \boldsymbol{c}^{(k)}_1 = [c^{(k)}_{1,1}, c^{(k)}_{1,2}, \dots, c^{(k)}_{1,M}]^T, \tag{36}$$

and

$$\boldsymbol{Q}^{(0)}_{\gamma_{T_0}} = \underbrace{[\boldsymbol{Q}_{\gamma_{T_0}} \boldsymbol{Ex}\boldsymbol{\psi}_{0,1}, \boldsymbol{Q}_{\gamma_{T_0}} \boldsymbol{Ex}\boldsymbol{\psi}_{0,2}, \dots, \boldsymbol{Q}_{\gamma_{T_0}} \boldsymbol{Ex}\boldsymbol{\psi}_{0,M}]}_{\text{matrix of } M \text{ columns}} \tag{37}$$

The remaining three matrices in (35), $\boldsymbol{Q}^{(1)}_{\gamma_{T_0}}$, $\boldsymbol{R}^{(0)}_{\gamma_{T_0}}$, and $\boldsymbol{R}^{(1)}_{\gamma_{T_0}}$, are constructed similar to (37). Each has the dimension of $|\gamma_{T_0}| \times M$, where $|\gamma_{T_0}|$ is the number of nodes in γ_{T_0}. We emphasize that, while the matrices (operators) $\boldsymbol{Q}^{(0)}_{\gamma_{T_0}}$, $\boldsymbol{Q}^{(1)}_{\gamma_{T_0}}$, $\boldsymbol{R}^{(0)}_{\gamma_{T_0}}$, and $\boldsymbol{R}^{(1)}_{\gamma_{T_0}}$ are derived from the difference projection $\boldsymbol{P}_{\gamma_t}$ of (31) that operates in the space of grid functions at the discrete boundary γ_t, the unknowns in equations (35) are the coefficients of the spectral expansion (26) defined on the continuous boundary Γ_t. Equations (35) represent a recursion for the coefficients (36) with respect to $k = 1, 2, \dots, K$ in a fully discrete framework.

4. Boundary equations with projections for vector unknowns

Equations (35) reduce the scalar wave equation (12) from the domain to the boundary. They are derived using the spectral discretization (26), finite-difference scheme (30), discrete BEP (32), and extension (33). It is important that no boundary conditions contribute to equations (35) at all. Boundary conditions will be taken into account separately (Section 5).

Consequently, an independent system of equations (35) can be written for each of the three Cartesian components of the electric field, E_x, E_y, and E_z, because each of these components satisfies the d'Alembert equation (12) on Ω_1 independently of the others. Moreover, as long as we use the same discretization for all three field components (same basis functions at the boundary, same volumetric grid and difference scheme, and same extension), the resulting boundary equations will be identical. They will merely need to be juxtaposed to form a system of boundary equations for the overall vector field $\boldsymbol{E} = (E_x, E_y, E_z)$.

Let us introduce the vectors of coefficients similar to (36) for each of the three field components: $\boldsymbol{c}^{(k)}_{0,x}$ and $\boldsymbol{c}^{(k)}_{1,x}$ for E_x, $\boldsymbol{c}^{(k)}_{0,y}$ and $\boldsymbol{c}^{(k)}_{1,y}$ for E_y, and $\boldsymbol{c}^{(k)}_{0,z}$ and $\boldsymbol{c}^{(k)}_{1,z}$ for E_z. Let us also build the combined $3M$-dimensional vectors (for every $k = 1, 2, \dots, K$):

$$\mathfrak{c}^{(k)}_0 = \begin{bmatrix} \boldsymbol{c}^{(k)}_{0,x} \\ \boldsymbol{c}^{(k)}_{0,y} \\ \boldsymbol{c}^{(k)}_{0,z} \end{bmatrix} \text{ and } \mathfrak{c}^{(k)}_1 = \begin{bmatrix} \boldsymbol{c}^{(k)}_{1,x} \\ \boldsymbol{c}^{(k)}_{1,y} \\ \boldsymbol{c}^{(k)}_{1,z} \end{bmatrix}, \tag{38}$$

as well as the combined block-diagonal operators of dimension $3|\gamma_{T_0}| \times 3M$:

$$\mathfrak{Q}^{(0)}_{\gamma_{T_0}} = \left[\begin{array}{c|c|c} \boldsymbol{Q}^{(0)}_{\gamma_{T_0}} & & \\ \hline & \boldsymbol{Q}^{(0)}_{\gamma_{T_0}} & \\ \hline & & \boldsymbol{Q}^{(0)}_{\gamma_{T_0}} \end{array}\right], \quad \mathfrak{Q}^{(1)}_{\gamma_{T_0}} = \left[\begin{array}{c|c|c} \boldsymbol{Q}^{(1)}_{\gamma_{T_0}} & & \\ \hline & \boldsymbol{Q}^{(1)}_{\gamma_{T_0}} & \\ \hline & & \boldsymbol{Q}^{(1)}_{\gamma_{T_0}} \end{array}\right],$$

$$\mathfrak{R}^{(0)}_{\gamma_{T_0}} = \left[\begin{array}{c|c|c} \boldsymbol{R}^{(0)}_{\gamma_{T_0}} & & \\ \hline & \boldsymbol{R}^{(0)}_{\gamma_{T_0}} & \\ \hline & & \boldsymbol{R}^{(0)}_{\gamma_{T_0}} \end{array}\right], \quad \mathfrak{R}^{(1)}_{\gamma_{T_0}} = \left[\begin{array}{c|c|c} \boldsymbol{R}^{(1)}_{\gamma_{T_0}} & & \\ \hline & \boldsymbol{R}^{(1)}_{\gamma_{T_0}} & \\ \hline & & \boldsymbol{R}^{(1)}_{\gamma_{T_0}} \end{array}\right]. \tag{39}$$

Note that, the combined operators (39) do not require any extra computations beyond those needed for the individual columns of the single-component matrices $\boldsymbol{Q}^{(0)}_{\gamma_{T_0}}$, $\boldsymbol{Q}^{(1)}_{\gamma_{T_0}}$, $\boldsymbol{R}^{(0)}_{\gamma_{T_0}}$, and $\boldsymbol{R}^{(1)}_{\gamma_{T_0}}$, see (37). Each column requires one solution of the AP (30). Then, the resulting single-component matrices become blocks in (39) with no additional computations necessary.

Given the definitions (38) and (39), we derive from (35):

$$\mathfrak{Q}^{(0)}_{\gamma_{T_0}} \mathfrak{c}^{(1)}_0 + \mathfrak{Q}^{(1)}_{\gamma_{T_0}} \mathfrak{c}^{(1)}_1 = \boldsymbol{0}, \quad k = 1, \tag{40a}$$

$$\mathfrak{Q}^{(0)}_{\gamma_{T_0}} \mathfrak{c}^{(k)}_0 + \mathfrak{Q}^{(1)}_{\gamma_{T_0}} \mathfrak{c}^{(k)}_1 = -\mathfrak{R}^{(0)}_{\gamma_{T_0}} \mathfrak{c}^{(k-1)}_0 - \mathfrak{R}^{(1)}_{\gamma_{T_0}} \mathfrak{c}^{(k-1)}_1, \quad k = 2, \dots, K. \tag{40b}$$

Equations (40) extend the recursion (35) from the case of a scalar unknown to the case of a 3D vector unknown. As before, the update for every k reduces to taking the previously determined coefficients as data for the next step, while all the operators remain k-independent. Of course, with no boundary conditions the solution to equations (40) is not unique. Moreover, the equations for different field components are still uncoupled (different blocks in (39)). In Section 5, we describe the implementation of the boundary conditions (7b)–(7c).

5. Collocation method for the boundary conditions

The boundary conditions (7b)–(7c) involve the values of the solution itself, as well as its first-order derivatives in space, at the scattering surface $\partial\Omega$. Hence, one can think of these boundary conditions as of relations between the boundary traces of the field components, $\boldsymbol{T}r_{\Gamma^{(k)}}E_x$, $\boldsymbol{T}r_{\Gamma^{(k)}}E_y$, and $\boldsymbol{T}r_{\Gamma^{(k)}}E_z$, as the solution is computed in time increments of length T_0 (see equations (27)). These relations will not depend on k, because nothing but the data $\boldsymbol{E}^{\text{imp}}$ in the boundary conditions (7b)–(7c) depends on time.

Boundary conditions (7b)–(7c) can be implemented in different coordinate systems. In this work, we choose a local surface-oriented frame of reference, as outlined in Section 3.4 after formula (33). The rationale is that, the impinging field (input data) is specified on the surface $\partial\Omega$ and surface-oriented coordinates appear very convenient for computing the divergence in (7c). Also, the normal to the surface automatically coincides with the third axis of this coordinate system. On the other hand, as the impinging field is given by its Cartesian components, a transformation needs to be known between the Cartesian components of a vector and components of the same vector in surface-oriented coordinates.

Consider a 3×3 transformation matrix $\boldsymbol{T}$ between the Cartesian components of a vector $\boldsymbol{E}$ and its components in the local frame:

$$\begin{bmatrix} E_{s_1} \\ E_{s_2} \\ E_{z'} \end{bmatrix} = \boldsymbol{T} \begin{bmatrix} E_x \\ E_y \\ E_z \end{bmatrix}.$$

The matrix $\boldsymbol{T}$ is defined on the scattering surface and depends on the specific location $\partial\Omega \ni \bar{\mathfrak{n}} = (s_1, s_2, z' = 0)$.[1] Then, boundary condition (7b) for the tangential components of the scattered field reads:

$$E_{s_i} = -E^{\text{imp}}_{s_i} = -[\boldsymbol{T}\boldsymbol{E}^{\text{imp}}]_{s_i} = -\boldsymbol{T}_{s_i j}E^{\text{imp}}_j, \quad i = 1, 2, \tag{41}$$

where $j = x, y, z$. Hereafter, summation over the repeated indices is assumed.

Boundary condition (7c) in the local frame of reference is

$$\text{div}\boldsymbol{E} = \partial_i E^i + \Gamma^j_{ji}E^i = 0,$$

where ∂_i denotes $\partial/\partial s_1$, $\partial/\partial s_2$, and $\partial/\partial z'$, the contravariant components E^i of the scattered field $\boldsymbol{E}$ are E_{s_1}, E_{s_2}, and $E_{z'}$, and Γ^j_{ji} are the Christoffel coefficients convoluted over the repeated indices. Since the tangential components E_{s_i} are specified by (41), their derivatives $\partial E_{s_i}/\partial s_i = -\partial E^{\text{imp}}_{s_i}/\partial s_i$, $i = 1, 2$, can be considered given on $\partial\Omega$. Hence, we have:

$$\frac{\partial E_{z'}}{\partial z'} + \Gamma^j_{jz'}E_{z'} = \sum_{i=1}^{2}\left(\frac{\partial E^{\text{imp}}_{s_i}}{\partial s_i} + \Gamma^j_{js_i}E^{\text{imp}}_{s_i}\right), \tag{42}$$

where all the unknown quantities are gathered on the left-hand side of (42), while the right-hand side of (42) is known.

Using (41) and a similar relation for the normal component of the field, $E_{z'} = [\boldsymbol{T}\boldsymbol{E}]_{z'}$, we derive from (42):

$$\left(\frac{\partial}{\partial z'} + \Gamma^j_{jz'}\right)[\boldsymbol{T}\boldsymbol{E}]_{z'} = \sum_{i=1}^{2}\left(\frac{\partial}{\partial s_i} + \Gamma^j_{js_i}\right)[\boldsymbol{T}\boldsymbol{E}^{\text{imp}}]_{s_i}. \tag{43}$$

The derivatives of the Cartesian components of the field with respect to the local coordinates in (43) are computed by the chain rule, e.g., $\frac{\partial E_x}{\partial s_i} = \frac{\partial E_x}{\partial x}\frac{\partial x}{\partial s_i} + \frac{\partial E_x}{\partial y}\frac{\partial y}{\partial s_i} + \frac{\partial E_x}{\partial z}\frac{\partial z}{\partial s_i}$, where $\frac{\partial x}{\partial s_i}$, etc., are known from the mapping (10). In addition, formula (43) implies differentiation not only of the fields but also the transformation matrix $\boldsymbol{T} = \boldsymbol{T}(s_1, s_2, z')$. The corresponding derivatives are to be evaluated at $(s_1, s_2, z' = 0)$, i.e., on the surface $\partial\Omega$.

Equations (41) and (43) represent the boundary conditions (7b)–(7c) at any location on the surface of the scatterer. We apply these equations at a chosen set of collocation points. Consider one such point on the patch P_j with the parametric coordinates $(s_1, s_2) \in \hat{P}_j$, see formulae (9)–(10). Let also $(k-1)T_0 < t \leqslant kT_0$ be the current moment of time. Define the following matrix of dimension $3\times 3M$:

[1] This matrix is the inverse of the matrix that relates the basis vectors in the two coordinate systems: $[\boldsymbol{\tau}_1, \boldsymbol{\tau}_2, n] = [e_x, e_y, e_z]\boldsymbol{T}^{-1}$.

$$\boldsymbol{\Psi} = \boldsymbol{\Psi}(s_1, s_2, t) = \left[\begin{array}{c|c|c} \psi_1(\cdot)\ \cdots\ \psi_M(\cdot) & & \\ \hline & \psi_1(\cdot)\ \cdots\ \psi_M(\cdot) & \\ \hline & & \psi_1(\cdot)\ \cdots\ \psi_M(\cdot) \end{array}\right]\Bigg\|_{(s_1,s_2,t-(k-1)T_0)}, \tag{44}$$

where $\psi_1, \ldots, \psi_M$ are the basis functions, see Section 3.4. Then, using formulae (26) and (38), we can represent the electric field $\boldsymbol{E} = (E_x, E_y, E_z)$ and its normal derivative at (s_1, s_2, t) as

$$\boldsymbol{E} = \boldsymbol{\Psi}\mathfrak{c}_0^{(k)}, \quad \frac{\partial}{\partial z'}\boldsymbol{E} = \boldsymbol{\Psi}\mathfrak{c}_1^{(k)}. \tag{45}$$

Formulae (41), (44), and (45) allow us to recast the boundary condition (7b) for the two tangential components of the scattered field at (s_1, s_2, t) as follows:

$$\mathfrak{b}_{s_i}^{(0)}\mathfrak{c}_0^{(k)} = -[\boldsymbol{T}\boldsymbol{E}^{\mathrm{imp}}(s_1, s_2, t)]_{s_i}, \quad i = 1, 2, \tag{46}$$

where $\boldsymbol{E}^{\mathrm{imp}}(s_1, s_2, t)$ is known and $\mathfrak{b}_{s_i}^{(0)} \equiv [\boldsymbol{T}\boldsymbol{\Psi}]_{s_i}$ is a $1 \times 3M$ row vector equal to the row # i of the $3 \times 3M$ matrix $\boldsymbol{T}\boldsymbol{\Psi}$ that corresponds to the local coordinate s_i.

Equations (46) hold at a specific collocation point $(s_1, s_2) \in \hat{P}_j$ and moment of time $(k-1)T_0 < t \leqslant kT_0$. Similar equations can be obtained for all chosen collocation points and moments of time. Combining the resulting equations, i.e., literally "stacking" them on top of one another, we arrive at two sets of equations for $\mathfrak{c}_0^{(k)}$ as per the two independent tangential directions of the local frame of reference:

$$\mathfrak{B}_{s_i}^{(0)}\mathfrak{c}_0^{(k)} = \Big\{ -[\boldsymbol{T}\boldsymbol{E}^{\mathrm{imp}}(s_1, s_2, t)]_{s_i} \Big\}_{\substack{\text{collocation}\\ \text{points/times}}} \tag{47}$$

where $\mathfrak{B}_{s_i}^{(0)}$ is composed of the rows $\mathfrak{b}_{s_i}^{(0)}$ for all collocation points/times. The notation on the right-hand side of equation (47) implies that the data shall be taken at the corresponding collocation points and moments of time.

Likewise, equations (43)–(45) lead to the following relations for the coefficients $\mathfrak{c}_0^{(k)}$, $\mathfrak{c}_1^{(k)}$:

$$[\mathfrak{B}_{z'}^{(1)} + \boldsymbol{\Gamma}_{jz'}^{j}\mathfrak{B}_{z'}^{(0)}]\mathfrak{c}_0^{(k)} + \mathfrak{B}_{z'}^{(0)}\mathfrak{c}_1^{(k)} = \left\{ \sum_{i=1}^{2} \left(\frac{\partial}{\partial s_i} + \Gamma_{js_i}^{j} \right) [\boldsymbol{T}\boldsymbol{E}^{\mathrm{imp}}]_{s_i} \right\}_{\substack{\text{collocation}\\ \text{points/times}}} \tag{48}$$

where $\mathfrak{B}_{z'}^{(0)}$ and $\mathfrak{B}_{z'}^{(1)}$ consist of the row vectors $\mathfrak{b}_{z'}^{(0)} \equiv [\boldsymbol{T}\boldsymbol{\Psi}]_{z'}$ and $\mathfrak{b}_{z'}^{(1)} \equiv [\frac{\partial \boldsymbol{T}}{\partial z'}\boldsymbol{\Psi}]_{z'}$ for all the collocation points/times, respectively. Note that, the Christoffel coefficients depend on the location is space. Accordingly, the quantities $\Gamma_{js_i}^{j}$ on the right-hand side of equation (48) shall be attributed to specific collocation points. On the left-hand side of equation (48), $\boldsymbol{\Gamma}_{jz'}^{j}$ represents a diagonal matrix of appropriate dimension with location-specific coefficients $\Gamma_{jz'}^{j}$ as entrees.

We emphasize that the matrix $\boldsymbol{T}$ depends only on the location in space, while the matrix $\boldsymbol{\Psi}$ depends on the location in space and the moment of time within the interval $[0, T_0]$, but does not depend on k (see formula (44) and recall that the basis functions in Section 3.4 were defined on the time interval $[0, T_0]$). Consequently, the operators $\mathfrak{B}_{s_i}^{(0)}$, $\mathfrak{B}_{z'}^{(0)}$, and $\mathfrak{B}_{z'}^{(1)}$ in equations (47)–(48) do not depend on k either.

The choice of the collocation points and times presents a separate question. Many strategies can be explored. In the current work, the collocation points coincide with the points $\bar{\mathfrak{n}} \in \partial\Omega$ used for constructing the extension operator (33), i.e., with the feet of the normals dropped from the nodes $\mathfrak{n} \in \gamma$ onto $\partial\Omega$. The collocation times coincide with the discretization levels of the finite-difference scheme (Section 3.4). Then, the overall number of equations in three sets (47)–(48) that represent the boundary conditions (7b)–(7c) on $\Gamma^{(k)}$ is $3|\gamma_{T_0}|$. Moreover, let's note that all time-independent constructs such as $\boldsymbol{T}$, the differentiated matrices $\frac{\partial}{\partial s_i}\boldsymbol{T}$, $\frac{\partial}{\partial z'}\boldsymbol{T}$, the Christoffel symbols, etc., need to be computed at the collocation points ahead of time and only once, when building the geometric model and computational grid. Technically, this computation relies on a computer algebra system.

The boundary conditions (47)–(48) supplement the recursion (40):

$$\left[\begin{array}{c|c} \mathfrak{Q}_{\gamma_{T_0}}^{(0)} & \mathfrak{Q}_{\gamma_{T_0}}^{(1)} \\ \hline \mathfrak{B}_{s_1}^{(0)} & \boldsymbol{0} \\ \hline \mathfrak{B}_{s_2}^{(0)} & \boldsymbol{0} \\ \hline \mathfrak{B}_{z'}^{(1)} + \boldsymbol{\Gamma}_{jz'}^{j}\mathfrak{B}_{z'}^{(0)} & \mathfrak{B}_{z'}^{(0)} \end{array}\right] \left[\begin{array}{c} \mathfrak{c}_0^{(k)} \\ \mathfrak{c}_1^{(k)} \end{array}\right] = \left[\begin{array}{c} -\mathfrak{R}_{\gamma_{T_0}}^{(0)}\mathfrak{c}_0^{(k-1)} - \mathfrak{R}_{\gamma_{T_0}}^{(1)}\mathfrak{c}_1^{(k-1)} \\ \mathfrak{d}^{(k)} \end{array}\right], \tag{49}$$

where the vector $\mathfrak{d}^{(k)}$ represents the combined data from the right-hand sides of equations (47) and (48). The three bottom rows of blocks in the matrix on the left-hand side of equation (49) correspond to the boundary conditions (7b)–(7c) and thus render the coupling between the Cartesian components of the electric field $\boldsymbol{E}$ at the surface of the scatterer.

Equation (49) shall be solved in the sense of least squares. As the matrix on the left-hand side of equation (49) does not depend on k, it can be QR-factorized ahead of time so that the final form of the time-marching algorithm with respect to k becomes:

$$\begin{bmatrix} \mathfrak{c}_0^{(k)} \\ \mathfrak{c}_1^{(k)} \end{bmatrix} = \underbrace{-\mathcal{R}^{-1}\mathcal{Q}^* \begin{bmatrix} \mathfrak{R}_{\gamma_{T_0}}^{(0)} & \mathfrak{R}_{\gamma_{T_0}}^{(1)} & \boldsymbol{0} \\ \boldsymbol{0} & \boldsymbol{0} & \boldsymbol{I} \end{bmatrix}}_{\text{transition matrix}} \begin{bmatrix} \mathfrak{c}_0^{(k-1)} \\ \mathfrak{c}_1^{(k-1)} \\ \mathfrak{d}^{(k)} \end{bmatrix}. \tag{50}$$

The transition matrix on the right-hand side of equation (50) is obtained via QR-factorization of the matrix on the left-hand side of equation (49). We compute the factorization using the Math Kernel Library (MKL) from Intel®. This library is optimized for the architecture and renders internal parallelization. For the specific dimensions used for simulations in Section 6, the computational cost of QR-factorization appears negligible on our 32-core Dell PowerEdge server with two Intel® Xeon® CPU E5-2698 v3 2.30 GHz processors and 512 Gb of RAM.

6. Numerical simulations

For each of our test cases (see Sections 6.1 and 6.2), we first need to choose the basis ψ_m, $m = 1, \ldots, M$, for the spectral expansion (26) at the space-time boundary Γ_t, as well as the finite-difference grid. The overall error of numerical solution is affected by both the error at the boundary and the error on the grid. For large dimensions of the basis M the spectral expansion error at the boundary is small and the finite-difference error dominates, while for moderate M's and sufficiently fine grids it is the other way around.

Therefore, an efficient strategy for choosing the dimension M is to analyze the accuracy of representing the boundary data, i.e., the impinging field (see formulae (7b)–(7c) and (41), (43)) in the form of an expansion w.r.t. the basis $\{\psi_m\}$. Indeed, the accuracy of representing the actual solution is expected to be the same. Then, on fine grids the error at the boundary will be dominant while on a sequence of coarser grids one will be able to observe the grid convergence until the finite-difference error reaches the level of the boundary error.

6.1. Sphere

Consider a unit PEC sphere centered at the origin and illuminated by a plane EM wave with the electric component $\boldsymbol{E}^{\text{imp}} = \boldsymbol{e}_x \cos(\boldsymbol{k}\boldsymbol{x} - \omega t)$. The incident field propagates along the z-axis, $\boldsymbol{k} = k\boldsymbol{e}_z$, and is linearly polarized along the x-axis. A series solution for the scattered field is known and expressed using vector spherical harmonics (see, e.g., [33, Chapter 13]). Taking sufficiently many terms in the series, we obtain a reference solution that the numerical results can be compared against. The domain where the scattered field is sought for is a cube $[-1.5, 1.5]^3$ that contains the scatterer (unit sphere). A larger computational domain for solving the auxiliary problem (28) is a cube $[-4.7, 4.7]^3$ truncated by the simplest homogeneous boundary conditions. The size of this domain is chosen so that the signal reflected from its boundaries won't reach the domain of interest $[-1.5, 1.5]^3$ during the interval of time when the AP is solved. The computational domain is discretized by a $77 \times 77 \times 77$ uniform Cartesian grid with size $h_x = h_y = h_z$ such that the diameter of the sphere is 14 cells. This grid is partially visualized in Fig. 3. It will subsequently be referred to as Grid 1x. The time step for integration is chosen as $h_t = h_x/3$. A twice as fine grid in both space and time will be called Grid 2x and used for studying the convergence.

We use two schemes for solving the AP (28): the standard second-order central difference explicit scheme and a fourth-order compact implicit scheme of [27] on the $3 \times 3 \times 3 \times 3$ space-time stencil. The fourth-order scheme first introduces the discretization in time:

$$\Delta u^{n+1} - \frac{u^{n+1}}{\theta\tau^2c^2} = 2\left(\Delta u^n - \frac{u^n}{\theta\tau^2c^2}\right) - \left(\Delta u^{n-1} - \frac{u^{n-1}}{\theta\tau^2c^2}\right) - \frac{1}{\theta}\Delta u^n, \tag{51}$$

where $\theta = \frac{1}{12}$. Equation (51) is a modified Helmholtz equation $\Delta u^{n+1} - \kappa^2 u^{n+1} = f^{n+1}$ on the upper time level. It is discretized by fourth-order compact finite differences in space [27].

The sphere does not require multiple patches. It is parameterized in its entirety according to (8) so that $s_1 = \theta$ and $s_2 = \varphi$. The basis functions introduced in Section 3.4 for the spectral representation of the field (26) are taken as products of spherical harmonics $Y_{lm}(\theta, \varphi)$ and Chebyshev polynomials $T_n(t)$: $\psi_i = \psi_i(\theta, \varphi, t) = Y_{lm}(\theta, \varphi)T_n(t)$, $i = 1, \ldots, M$. The choice of the dimension M in the case of a sphere is discussed in detail in our earlier work [2], see, in particular [2, Tables 5 and 6], and the same considerations apply here without any change.

In Fig. 1 and Table 1, we demonstrate the stability and convergence of computations over a long simulation time, on the order of $1000 \times \frac{\text{diameter of the sphere}}{\text{propagation speed}}$. The impinging wavelength is approximately equal to the radius of the sphere, $\lambda \approx 1$. The number of spherical harmonics is $L_{\max} = 7$ and the number of Chebyshev polynomials is $N_{\max} = 6$, so the dimension of the basis is $M = (1 + L_{\max})^2(1 + N_{\max}) = 448$. Fig. 1 and Table 1 show that the numerical solution converges to the reference solution with the design second-order rate.

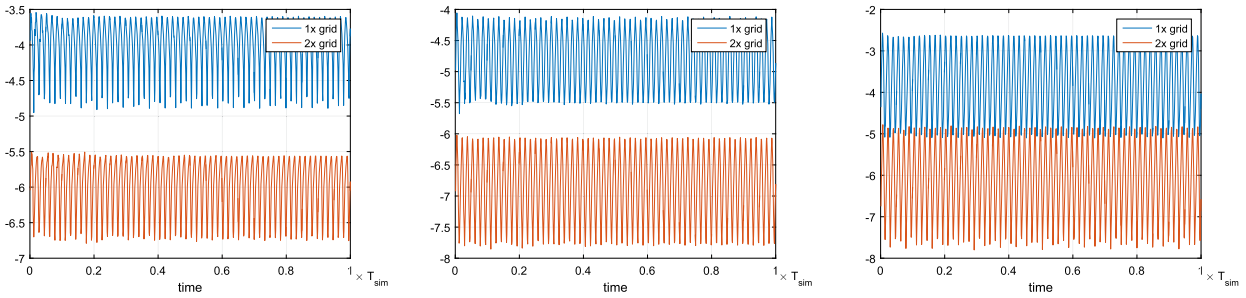

(a) E_x (b) E_y (c) E_z

Fig. 1. $\log_2 \|\text{relative error}\|_\infty$ vs. time, second-order accurate central scheme.

Table 1
Average relative error and convergence rate, second-order accurate central scheme.

Grid	E_x		E_y		E_z	
	Error	Rate	Error	Rate	Error	Rate
1x	0.0641	–	0.0379	–	0.0851	–
2x	0.0162	3.95	0.00998	3.80	0.0225	3.78

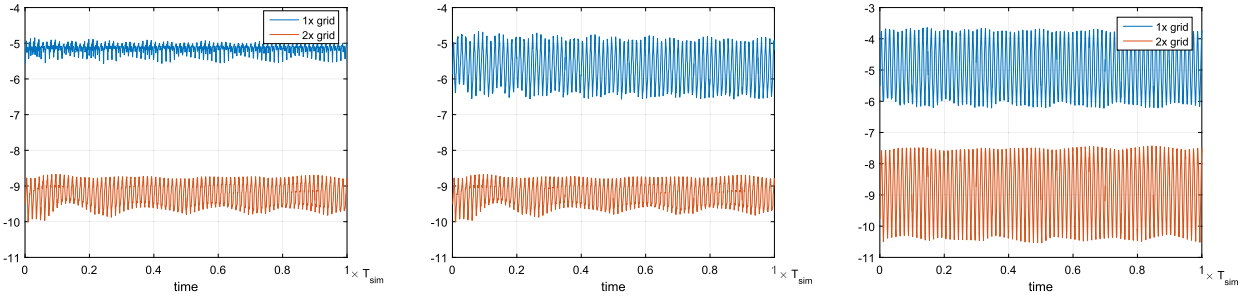

(a) E_x (b) E_y (c) E_z

Fig. 2. $\log_2 \|\text{relative error}\|_\infty$ vs. time, fourth-order accurate compact scheme.

Table 2
Average relative error and convergence rate, fourth-order accurate compact scheme.

Grid	E_x		E_y		E_z	
	Error	Rate	Error	Rate	Error	Rate
1x	0.0283	–	0.0209	–	0.0378	–
2x	0.00181	15.6	0.00139	15.1	0.00227	16.6

Fig. 2 and Table 2 are counterparts to Fig. 1 and Table 1, respectively, but for the fourth-order accurate scheme. Stability and the design convergence rate can be observed.

Finally, in Fig. 3 we present several cross-sections of the field for a fixed moment of time. Compared to the simulations of Figs. 1 and 2 (and Tables 1 and 2), the wavelength is twice as short, $\lambda \approx 1/2$, and a larger basis is used: $L_{\max} = 11$, $N_{\max} = 8$.

6.2. *Double-cone hypersonic shape*

6.2.1. *Setup*

Consider a double-cone shape shown in Fig. 4. Shapes of this type are often used for hypersonic CFD simulations [39]. We will compute the EM scattering about this shape. The double-cone shown in Fig. 4 has been created using the Rhinoceros 3D© CAD software. The bounding box in Fig. 4(a) is the domain where the scattered field is to be computed.

To construct a spline-defined double-cone shown in Fig. 4, we use the topologically quadrilateral 2D NURBS patches parametrized by two variables (see equations (9)–(10)). The patches are made periodic in one direction by matching the corresponding opposite edges. In general, the way the patches are created, manipulated, and assembled into the final object is case-specific, relies on the capabilities of the CAD software, and requires a lot of technical details. Specifically in the double-cone case, we first define a generatrix composed of straight segments and then revolve it about the axis of symmetry using CAD. The resulting surface is

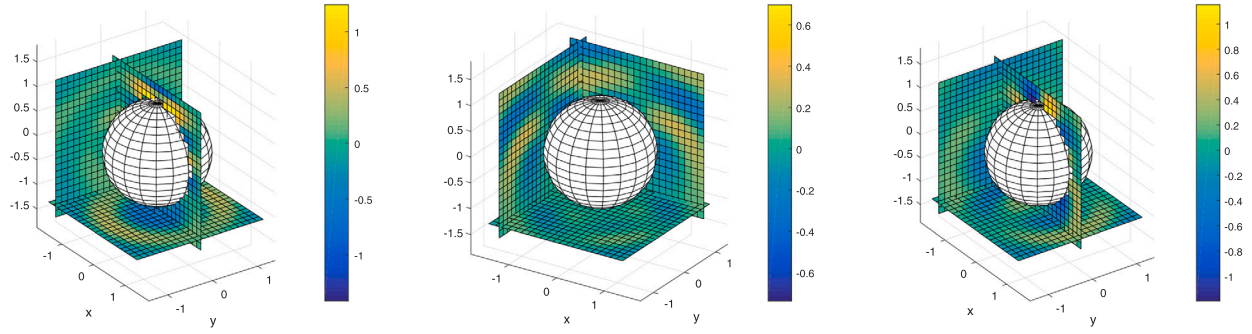

(a) E_x (b) E_y (c) E_z

Fig. 3. Cross-sections of the scattered field for a fixed moment of time.

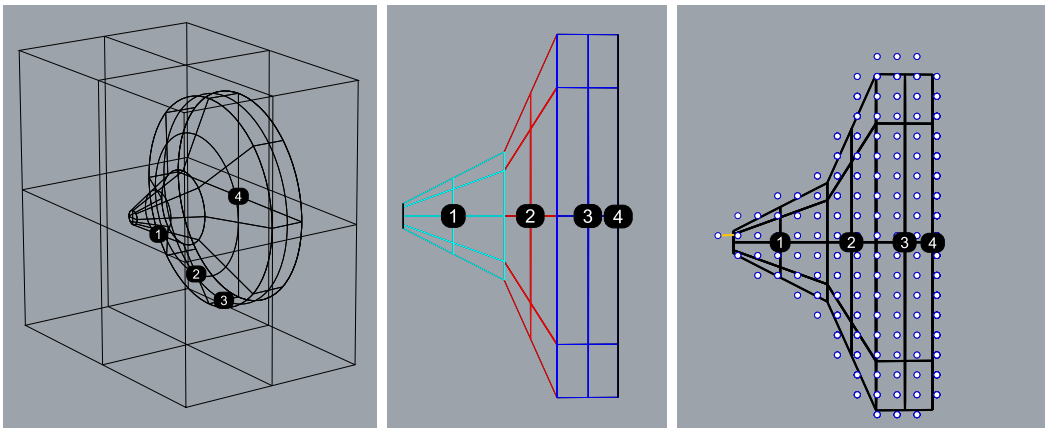

(a) The scatterer and the domain where the field is computed (b) Four patches (c) Oblique extension (shown by yellow segment)

Fig. 4. Hypersonic double-cone scattering shape. (For interpretation of the colors in the figure(s), the reader is referred to the web version of this article.)

a 2D piecewise NURBS that employs first-order splines in the longitudinal direction (the generatrix is piecewise linear) and fifth-order splines in the other, periodic direction. The overall surface is split into patches # 1, 2, and 3 by isolines (lines for which the parametric variable aligned with the main axis of the object is constant) at the knots of the piecewise linear generatrix. Then, the opening at the base of the cylindrical patch (patch # 3) is capped by a regular planar quadrilateral patch. The CAD software trims it at the intersection curve with the hull (a circle) leaving what we see in Fig. 4 as patch # 4. Trimming means dividing the domain of parameters into the active and inactive parts of the quadrilateral. The inactive part is visually removed but mathematically the patch remains a rectangle. In Fig. 4(b), the four patches that define the double-cone are identified by color.

There is also a planar cap at the tip of the front cone (patch # 1). This cone is truncated intentionally to avoid a potential singularity in the surface representation at the vertex, which may render the Taylor-based extension $\boldsymbol{Ex}$ inaccurate if a node from γ is projected onto the vertex of very close to it. As a simple remedy, we extend the boundary data from the surface points located a little further away from the vertex, which yields an oblique extension, see Fig. 4(c). Hence, the front planar cap merely makes the overall hull closed ("waterproof"), which is important, e.g., for distinguishing between the interior and exterior points with the help of CAD algorithms. This cap is not used for building the extension $\boldsymbol{Ex}$.

Instead of a piecewise linear generatrix, we could have employed a smooth one thus obtaining a smoother shape with no sharp edges between the patches. In this case, however, the curvature of the surface would be high in the transition areas between the patches, i.e., near the current edges (see Fig. 4). That, in turn, might slow down the convergence of the spectral expansions at the boundary (see equations (26)), which effectively implies that more basis functions are needed. On the other hand, the algorithm of difference potentials involves no special treatment in the areas near the interfaces between the patches. This is true even in the case of sharp edges, like in Fig. 4.

No analytic solution is known for the scattering about the shape shown in Fig. 4. We therefore compute two different cases. The first one corresponds to an "engineered" reference solution that allows us to explicitly evaluate the error. The second one presents a more realistic scenario where an impinging plane wave is scattered about the double-cone.

Table 3
The error of spectral representation of the plane wave boundary data as it decreases when the basis dimension is successively doubled. Basis $1 = [1,3,4,2] \times [4,2,2,2] \times 8$, where the notation is $[n_1^{(1)},...,n_1^{(4)}] \times [n_2^{(1)},...,n_2^{(4)}] \times n_3$. Basis $2 = 2 \times$ Basis 1. Basis $3 = 2 \times$ Basis 2.

Patch #	Basis 1		Basis 2		Basis 3	
	error $u\|_\Gamma$	error $\frac{\partial u}{\partial n}\Big\|_\Gamma$	error $u\|_\Gamma$	error $\frac{\partial u}{\partial n}\Big\|_\Gamma$	error $u\|_\Gamma$	error $\frac{\partial u}{\partial n}\Big\|_\Gamma$
1	$2.1 \cdot 10^{-1}$	$3.2 \cdot 10^{-1}$	$2.3 \cdot 10^{-2}$	$3.3 \cdot 10^{-2}$	$3.0 \cdot 10^{-4}$	$7.7 \cdot 10^{-4}$
2	$5.1 \cdot 10^{-2}$	$1.0 \cdot 10^{-1}$	$7.2 \cdot 10^{-3}$	$4.5 \cdot 10^{-3}$	$6.2 \cdot 10^{-7}$	$2.4 \cdot 10^{-6}$
3	$1.2 \cdot 10^{-1}$	$1.5 \cdot 10^{-1}$	$3.0 \cdot 10^{-4}$	$8.2 \cdot 10^{-4}$	$2.0 \cdot 10^{-6}$	$1.2 \cdot 10^{-6}$
4	$0.9 \cdot 10^{-1}$	$1.1 \cdot 10^{-1}$	$2.6 \cdot 10^{-4}$	$3.3 \cdot 10^{-4}$	$1.4 \cdot 10^{-11}$	$2.0 \cdot 10^{-11}$

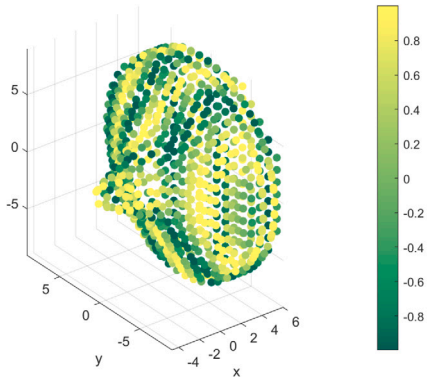

(a) Trace of the impinging field

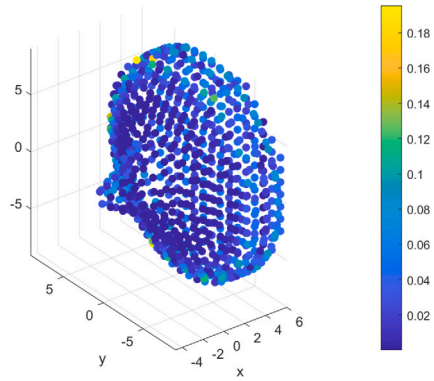

(b) Error of spectral representation

Fig. 5. A plane wave impinging on the double-cone at 45° with respect to its main axis. $D/\lambda \approx 4.25$, where D is the diameter and λ is the wavelength.

Table 4
Patch 1.

D/λ	$n_1^{(1)}$	$n_2^{(1)}$	n_3	# APs	error u	error $\frac{\partial u}{\partial n}$
≈ 1.5	1	4	8	135	0.21	0.32
≈ 2	2	2	10	165	0.09	0.09
≈ 2.75	5	3	12	572	0.17	0.04
≈ 4.25	8	5	16	1734	0.08	0.03

To engineer the reference solution, we place an artificial point dipole oriented along the z-axis inside the double-cone. The trace of the field radiated by this dipole (tangential components) is taken as boundary data on the surface of the double-cone. Then, the reference solution outside the shape is the dipole field itself:

$$E_r = 2\cos\theta\left(\frac{1}{r^2} - \frac{ik}{r}\right)\Pi_0, \quad E_\theta = \sin\theta\left(\frac{1}{r^2} - \frac{ik}{r} - k^2\right)\Pi_0, \quad \Pi_0 = \frac{1}{r}e^{ikr - i\omega t}. \tag{52}$$

For the scattering of a plane wave, the important parameters are the angle of incidence and the frequency. We first use the boundary data due to the impinging plane wave for analyzing the error of the spectral expansion at the boundary and choosing the dimension of the basis M. For patches 1, 2, and 3, the basis on the surface employs the trigonometric functions, $1, \cos s_1, \sin s_1, \cos 2s_1, \sin 2s_1, ..., \cos n_1^{(p)} s_1, \sin n_1^{(p)} s_1$ in the periodic direction and Chebyshev polynomials, $T_0(s_2), T_1(s_2), ..., T_{n_2^{(p)}}(s_2)$ in the longitudinal direction (that of generatrices). Patch 4 (back base in Fig. 4(b)) is a trimmed plane where Chebyshev's polynomials are used in both directions. For the results in this section, we will be using the following notation for the dimension of the basis: $[n_1^{(1)},...,n_1^{(4)}] \times [n_2^{(1)},...,n_2^{(4)}]$, where the numbers $n_1^{(p)}$ and $n_2^{(p)}$ define the basis dimension on patch $\#p$ in the directions s_1 and s_2, respectively. The basis in time consists of the Chebyshev's polynomials, $T_0(t)$, $T_1(t)$,...,$T_{n_3}(t)$.

In Table 3, we analyze the effect of varying the dimension of the basis on the surface of the double-cone scatterer. Depending on the patch, the error of the spectral expansion drops by a factor of 10 to 1000 as the dimension is doubled. Fig. 5 shows the impinging field to be expanded on the surface and the respective error.

In Tables 4–7, we investigate what dimension of the basis is required to keep the spectral representation error approximately constant while increasing the frequency of the impinging field. The diameter of the double-cone is denoted by D, and λ is the wavelength. The number of APs (30) to be solved due to patch p is $\#\text{APs} = (2n_1^{(p)} + 1)(n_2^{(p)} + 1)(n_3 + 1)$.

Given that the length of the double-cone is 11 units while its full diameter is $D = 18$ units, the computational domain for the AP (28) is taken as $[-25, 25] \times [-30, 30] \times [-30, 30]$ to guarantee that no reflections will contaminate the solution. A coarse grid (Grid 1x) of $46 \times 58 \times 58$ nodes on the computational domain is partially shown in Fig. 8. A finer grid (Grid 2x) contains twice as many nodes in each direction.

Table 5
Patch 2.

D/λ	$n_1^{(2)}$	$n_2^{(2)}$	n_3	# APs	error u	error $\frac{\partial u}{\partial n}$
≈ 1.5	3	2	8	189	0.05	0.10
≈ 2	5	3	10	484	0.10	0.09
≈ 2.75	6	4	12	845	0.20	0.22
≈ 4.25	10	10	16	3927	0.20	0.08

Table 6
Patch 3.

D/λ	$n_1^{(3)}$	$n_2^{(3)}$	n_3	# APs	error u	error $\frac{\partial u}{\partial n}$
≈ 1.5	4	2	8	243	0.12	0.15
≈ 2	5	3	10	484	0.18	0.19
≈ 2.75	7	3	12	780	0.19	0.17
≈ 4.25	11	9	16	3910	0.09	0.08

Table 7
Patch 4.

D/λ	$n_1^{(4)}$	$n_2^{(4)}$	n_3	# APs	error u	error $\frac{\partial u}{\partial n}$
≈ 1.5	2	2	8	81	0.09	0.11
≈ 2	3	1	10	88	0.04	0.07
≈ 2.75	4	2	12	195	0.09	0.04
≈ 4.25	6	2	16	357	0.06	0.03

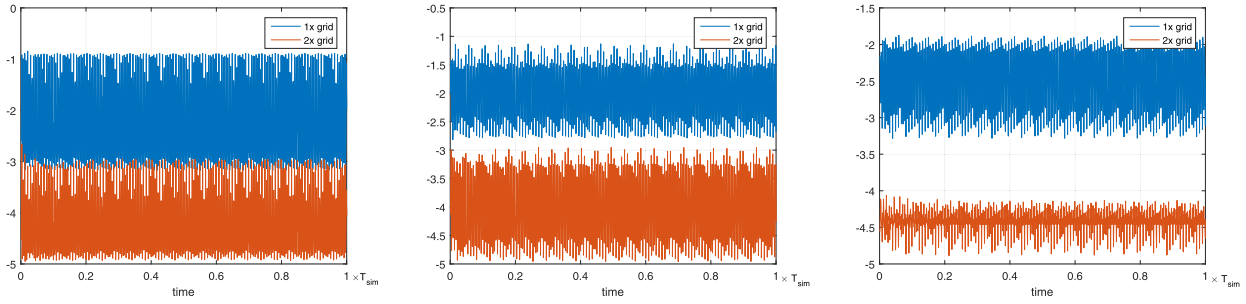

(a) E_x (b) E_y (c) E_z

Fig. 6. $\log_2 \|\text{relative error}\|_\infty$ vs. time, second-order accurate central scheme.

Table 8
Average errors and convergence rates for the second-order accurate central scheme. Basis dimension on the surface is $[4,4,4,6] \times [4,4,3,7]$ for Grid 1x and $[6,6,4,7] \times [7,5,5,8]$ for Grid 2x. Basis dimension in time is $n_3 = 7$.

Grid	E_x		E_y		E_z	
	Error	Rate	Error	Rate	Error	Rate
1x	0.242	–	0.259	–	0.191	–
2x	0.0631	3.83	0.0691	3.75	0.0492	3.88

6.2.2. Results

In the case of a reference solution (52), the error histories for $\lambda \approx 12$ over a long simulation time ($\sim 1000 \times \frac{\text{diameter of double-cone}}{\text{propagation speed}}$) are shown in Fig. 6. Table 8 summarizes the average errors and convergence rates. Long-term stability and the design rate of convergence of the algorithm are observed.

Similar computations have been conducted using the fourth-order compact scheme (51) (see [27] for detail) on two grids, Grid 1x of dimension $78 \times 90 \times 90$ and Grid 2x of twice as fine dimension. The results are presented in Fig. 7 and Table 9.

While the embedded dipole allows us to obtain the reference solution (52) and thus corroborate the convergence of the algorithm, it does not lead to a realistic scattering problem. Therefore, we also compute the scattering of a plane wave about the double-cone shown in Fig. 4. In Fig. 8, we present a snapshot of the resulting scattered field. The plane wave $\boldsymbol{E}^{\text{imp}} = \boldsymbol{E}_0 \cos(\boldsymbol{k}\boldsymbol{x} - \omega t)$ is linearly polarized along $\boldsymbol{E}_0 = (-0.5, -0.5, 1)/\sqrt{3/2}$ while its propagation direction defined by the wave vector $\boldsymbol{k} = \omega/c \cdot (1,1,1)/\sqrt{3}$ is orthogonal to $\boldsymbol{E}_0$. The wavelength in this case is the same as before, $\lambda \approx 12$, i.e., $D/\lambda \approx 1.5$.

We also note that, while the algorithm of difference potentials requires no adjustments for sharp edges between the patches (see Fig. 4), the solution itself may develop singularities at those edges. These singularities have nothing to do with any particular

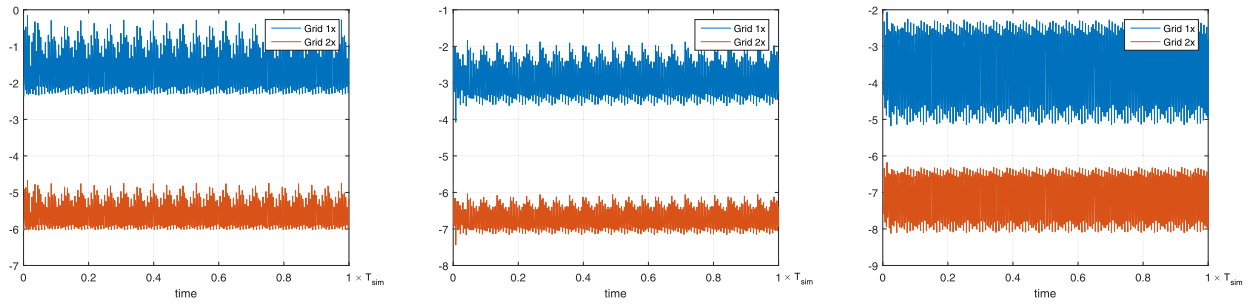

(a) E_x (b) E_y (c) E_z

Fig. 7. $\log_2 \|\text{relative error}\|_\infty$ vs. time, fourth-order accurate compact scheme.

Table 9
Average errors and convergence rates for the fourth-order accurate compact scheme. Basis dimension on the surface is $[6,6,4,11] \times [8,5,5,11]$. Basis dimension in time is $n_3 = 11$.

Grid	E_x		E_y		E_z	
	Error	Rate	Error	Rate	Error	Rate
1x	0.325	–	0.091	–	0.079	–
2x	0.021	15.63	0.0063	14.44	0.0053	14.91

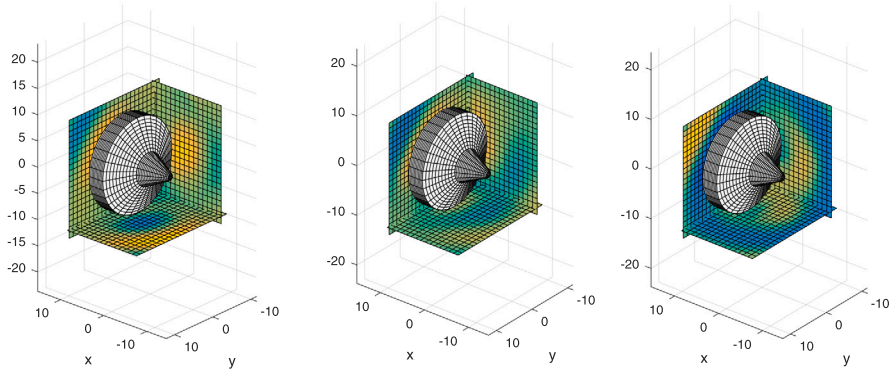

(a) E_x (b) E_y (c) E_z

Fig. 8. Cross-sections of the scattered field at a fixed moment of time as a plane wave impinges on the double-cone.

computational procedure. They rather characterize the solution of the differential equation per se and unless properly regularized, may slow down the finite-difference convergence (see, e.g., our earlier work on the Helmholtz equation [40]). In the current work, we do not propose any special treatment for these singularities. Indeed, a regularization would require knowing the asymptotic form of the solution near the singularity, which does not seem realistic in the case of a 3D scatterer of an arbitrary shape. We rather employ the MDP (enhanced by Huygens' principle) "as is" and expect that the rate of its grid convergence may be affected by singularities in the solution if they are sufficiently strong. On the other hand, the design rate of grid convergence demonstrated in Fig. 6 and Table 8 for a second-order accurate scheme and Fig. 7 and Table 9 for a fourth-order accurate scheme applies to the backward engineered test solution (52) which is not singular anywhere outside the scatterer including its boundary.

6.2.3. *Computational cost*

For the engineered reference solution (52) computed by means of a second-order accurate central difference scheme, the cost of one update of the spectral expansion coefficients at the boundary in accordance with equation (50) is $0.53 \cdot 10^{-2}$ seconds on grid 1x and $4.2 \cdot 10^{-2}$ seconds on grid 2x (on the same Dell PowerEdge server as described at the end of Section 5). The rate is 7.92. This cost still depends on the grid because the number of collocation points used for approximating the boundary conditions in the current implementation is equal to $|\gamma_{T_0}|$, see Section 5. In fact, the collocation points can be chosen independently of the grid and in that case the cost of the update (50) will also become grid independent, similar to what it was in our previous work [2,3] where we have used a Galerkin approximation of the boundary conditions. The cost of computing the solution on the entire domain at a given moment of time is 0.14 seconds on grid 1x and 1.12 seconds on grid 2x, so that the rate is 8.0. For the fourth-order accurate compact scheme (51), the corresponding costs of the update (50) are $0.76 \cdot 10^{-2}$ seconds on grid 1x and $5.8 \cdot 10^{-2}$ seconds on grid 2x with the rate of 7.6, while the costs of computing the solution are 0.15 seconds on grid 1x and 1.15 seconds on grid 2x, with the rate of

7.7. As all the rates are close to 8, we conclude that when the grid dimension is doubled, all costs scale roughly as 2^3 rather than 2^4, which would have been the case for the conventional volumetric time-marching.

7. Conclusions

Our numerical experiments fully corroborate the design properties of the proposed algorithm for solving the second-order Maxwell's equations. The algorithm provides high-order accuracy for general 3D geometries on Cartesian grids, demonstrates stability over arbitrarily long simulation times, and requires no special treatment of artificial outer boundaries.

The MDP reduces the problem from the domain to its boundary so that the time marching (50) is conducted along the boundary only. As the discrete Calderon's operators are precomputed ahead of time, multiple similar problems can be solved efficiently. In particular, changing the boundary conditions in Sections 6.1 and 6.2 does not require the new operators, only the data vectors $\mathfrak{d}^{(k)}$ on the right-hand side of (50) need to be updated. Computing the operators requires multiple solves of the AP (28) over a short interval of time $2T_0$. These solves are fully independent and efficiently implemented in parallel.

The dimension of the transition matrix on the right-hand side of (50) depends on the dimension of the spectral basis (26), as well as that of the collocation set used for approximating the boundary conditions (see Section 5). Fundamentally, this dimension does not have to depend on the grid, which would make the complexity of the time marching (50) fully grid-independent. This, in particular, is the case in [3], where we have used a Galerkin approach for implementing the boundary conditions. In this work, however, the collocation points on the surface $\partial\Omega$ are projections of the nodes from the grid boundary γ. Thus, the dimension of the collocation set still depends on the grid. In the future, we will consider other, more economical, strategies for defining the collocation set and making it grid-independent.

Long time stability of the proposed method has been consistently observed in all of our numerical experiments. We attribute it to the use of the strong Huygens' principle as a key component of the current algorithm (Section 3.3). In our earlier work [41], we proved a temporally uniform error bound in the case were we applied Huygens' principle to stabilizing the long time behavior of the various ABCs and PMLs (see also [42]). To extend the argument of [41, Section 7] to the problem analyzed in this paper, and thus rigorously establish the convergence seen in Figs. 1–2 and 6–7, a few additional steps are required. First, the proof of well-posedness of the boundary equations with projections given in [26, Part II, Section 1.2] will need to be adjusted to accommodate equation (13) and then (25). Then, the results originally due to Reznik (see [43,44] and also [26, Part III, Section 1.6]) on approximation of surface potentials of elliptic operators by difference potentials will need to be extended to the case of a wave equation considered on a finite non-increasing time interval (of duration $2T_0$). These theoretical developments will be a part of our future effort.

On the practical side of things, the potential extensions of the proposed method include the accommodation of additional geometries, use of the impedance boundary condition (5) rather than simplified PEC boundary condition (6), numerical solution of the true transmission/scattering problems, as well as the analysis of EM propagation in continuous media rather than only vacuum, which may involve variable speed c and/or source terms in the equations (charges and currents).

In the case of the impedance boundary condition, one needs to solve for both the electric and magnetic field. Then, the magnetic wave equation (3a) is discretized and replaced with the same recursive algorithm at the boundary as the electric wave equation (3b), see Sections 3 and 4. The impedance boundary condition (5) couples the tangential components of $\boldsymbol{H}$ and $\boldsymbol{E}$ and replaces the PEC condition (6), while the zero divergence condition on Γ has to hold for both $\boldsymbol{H}$ and $\boldsymbol{E}$. No ABCs are needed for either $\boldsymbol{E}$ or $\boldsymbol{H}$, because both wave equations (3) are Huygens'. The rationale is the same as discussed in Section 3.4.

To solve a full transmission/scattering problem, one shall build two MDP algorithms, one for the scattered EM field (exterior) and the other for the transmitted field (interior). The transmitted and scattered fields $\boldsymbol{H}$ and $\boldsymbol{E}$ are coupled at the boundary by the condition of continuity of their tangential components across the interface [5], while the divergence conditions are required to hold independently for each of the fields on each side of the interface. As before, no ABCs are needed for the exterior fields $\boldsymbol{H}$ and $\boldsymbol{E}$. To that end, we note that classical ABCs for Maxwell's equations, such as the Silver-Muller boundary conditions [36,37], couple the fields $\boldsymbol{H}$ and $\boldsymbol{E}$ at the artificial outer boundary. Our approach does not require any ABCs and thus allows one to avoid this coupling.

Of additional interest may be combined fluid/EM computations where the flow solver would determine the configuration of the plasma sheath around a hypersonic shape such as the one shown in Fig. 4 while the EM solver would subsequently compute the scattering of a given signal about the plasma layer. Another interesting application may be EM propagation through a human body.

CRediT authorship contribution statement

Sergey Petropavlovsky: Conceptualization, Formal analysis, Investigation, Methodology, Software, Visualization, Writing – original draft. **Semyon Tsynkov:** Conceptualization, Formal analysis, Funding acquisition, Investigation, Methodology, Project administration, Supervision, Writing – original draft, Writing – review & editing. **Eli Turkel:** Conceptualization, Formal analysis, Funding acquisition, Investigation, Methodology, Writing – original draft, Writing – review & editing.

Declaration of competing interest

The authors declare the following financial interests/personal relationships which may be considered as potential competing interests:

Eli Turkel reports financial support was provided by Binational Science Foundation, grant number 2020128.

Data availability

Data will be made available on request.

References

[1] S. Petropavlovsky, S. Tsynkov, E. Turkel, A method of boundary equations for unsteady hyperbolic problems in 3D, J. Comput. Phys. 365 (2018) 294–323, https://doi.org/10.1016/j.jcp.2018.03.039.

[2] S. Petropavlovsky, S.V. Tsynkov, E. Turkel, Numerical solution of 3D exterior unsteady wave propagation problems using boundary operators, SIAM J. Sci. Comput. 42 (2020) A3462–A3488, https://doi.org/10.1137/19M1269269.

[3] S. Petropavlovsky, S. Tsynkov, E. Turkel, 3D time-dependent scattering about complex shapes using high order difference potentials, J. Comput. Phys. 471 (2022) 111632, https://doi.org/10.1016/j.jcp.2022.111632.

[4] L.D. Landau, E.M. Lifshitz, Course of Theoretical Physics, vol. 2, the Classical Theory of Fields, fourth ed., Pergamon Press, Oxford, 1975, translated from the Russian by Morton Hamermesh.

[5] L.D. Landau, E.M. Lifshitz, Course of Theoretical Physics. Vol. 8, Electrodynamics of Continuous Media, Pergamon International Library of Science, Technology, Engineering and Social Studies, Pergamon Press, Oxford, 1984, Translated from the second Russian edition by J. B. Sykes, J. S. Bell and M. J. Kearsley, Second Russian edition revised by Lifshits and L. P. Pitaevskii.

[6] M.L. Levin, S.M. Rytov, V.D. Shafranov, M. A. Leontovich's researches in electrodynamics, Phys. Usp. 26 (1983) 353–355, https://doi.org/10.1070/PU1983v026n04ABEH004389, http://ufn.ru/en/articles/1983/4/e/.

[7] G. Pelosi, P.Y. Ufimtsev, The impedance-boundary condition, IEEE Antennas Propag. Mag. 38 (1996) 31–35, https://doi.org/10.1109/74.491289.

[8] A. Taflove, S.C. Hagness, Computational Electrodynamics: the Finite-Difference Time-Domain Method, third ed., Artech House Inc., Boston, MA, 2005.

[9] K.S. Yee, Numerical solution of initial boundary value problem involving Maxwell's equations in isotropic media, IEEE Trans. Antennas Propag. 14 (1966) 302–307.

[10] B. Yang, D. Gottlieb, J. Hesthaven, Spectral simulations of electromagnetic wave scattering, J. Comput. Phys. 134 (1997) 216–230, https://doi.org/10.1006/jcph.1997.5686, https://www.sciencedirect.com/science/article/pii/S0021999197956862.

[11] M. Cassier, P. Joly, M. Kachanovska, Mathematical models for dispersive electromagnetic waves: an overview, Comput. Math. Appl. 74 (2017) 2792–2830, https://doi.org/10.1016/j.camwa.2017.07.025.

[12] E. Bécache, M. Kachanovska, M. Wess, Convergence analysis of time-domain PMLs for 2D electromagnetic wave propagation in dispersive waveguides, ESAIM Math. Model. Numer. Anal. 57 (2023) 2451–2491, https://doi.org/10.1051/m2an/2023060.

[13] W.D. Henshaw, A high-order accurate parallel solver for Maxwell's equations on overlapping grids, SIAM J. Sci. Comput. 28 (2006) 1730–1765, https://doi.org/10.1137/050644379 (electronic).

[14] J.W. Banks, W.D. Henshaw, Upwind schemes for the wave equation in second-order form, J. Comput. Phys. 231 (2012) 5854–5889, https://doi.org/10.1016/j.jcp.2012.05.012.

[15] V. Dolean, M.J. Gander, E. Veneros, Schwarz methods for second order Maxwell equations in 3D with coefficient jumps, in: T. Dickopf, M.J. Gander, L. Halpern, R. Krause, L.F. Pavarino (Eds.), Domain Decomposition Methods in Science and Engineering XXII, Springer International Publishing, Cham, 2016, pp. 471–479.

[16] J.B. Angel, J.W. Banks, W.D. Henshaw, High-order upwind schemes for the wave equation on overlapping grids: Maxwell's equations in second-order form, J. Comput. Phys. 352 (2018) 534–567, https://doi.org/10.1016/j.jcp.2017.09.037.

[17] S.S. Neoh, F. Ismail, Time-explicit numerical methods for Maxwell's equation in second-order form, Appl. Math. Comput. 392 (2021) 125669, https://doi.org/10.1016/j.amc.2020.125669.

[18] M.J. Jenkinson, J.W. Banks, High-order accurate FDTD schemes for dispersive Maxwell's equations in second-order form using recursive convolutions, J. Comput. Appl. Math. 336 (2018) 192–218, https://doi.org/10.1016/j.cam.2017.12.016.

[19] J.B. Angel, J.W. Banks, W.D. Henshaw, M.J. Jenkinson, A.V. Kildishev, G. Kovačič, L.J. Prokopeva, D.W. Schwendeman, A high-order accurate scheme for Maxwell's equations with a generalized dispersive material model, J. Comput. Phys. 378 (2019) 411–444, https://doi.org/10.1016/j.jcp.2018.11.021.

[20] J.W. Banks, B.B. Buckner, W.D. Henshaw, M.J. Jenkinson, A.V. Kildishev, G. Kovačič, L.J. Prokopeva, D.W. Schwendeman, A high-order accurate scheme for Maxwell's equations with a generalized dispersive material (GDM) model and material interfaces, J. Comput. Phys. 412 (2020) 109424, https://doi.org/10.1016/j.jcp.2020.109424.

[21] J.B. Angel, J.W. Banks, A.M. Carson, W.D. Henshaw, Efficient upwind schemes for linear and nonlinear dispersive Maxwell's equations on overset grids, in: 2023 International Applied Computational Electromagnetics Society Symposium (ACES), 2023, pp. 1–2.

[22] H.-O. Kreiss, N.A. Petersson, J. Ystrom, Difference approximations for the second order wave equation, SIAM J. Numer. Anal. 40 (2002) 1940–1967, https://doi.org/10.1137/S0036142901397435.

[23] H.-O. Kreiss, N.A. Petersson, J. Ystrom, Difference approximations of the Neumann problem for the second order wave equation, SIAM J. Numer. Anal. 42 (2004) 1292–1323, https://doi.org/10.1137/S003614290342827X.

[24] S. Nilsson, N.A. Petersson, B. Sjögreen, H.-O. Kreiss, Stable difference approximations for the elastic wave equation in second order formulation, SIAM J. Numer. Anal. 45 (2007) 1902–1936, https://doi.org/10.1137/060663520.

[25] H.-O. Kreiss, O.E. Ortiz, N.A. Petersson, Initial-boundary value problems for second order systems of partial differential equations, ESAIM Math. Model. Numer. Anal. 46 (2012) 559–593, https://doi.org/10.1051/m2an/2011060.

[26] V.S. Ryaben'kii, Method of Difference Potentials and Its Applications, Springer Series in Computational Mathematics, vol. 30, Springer-Verlag, Berlin, 2002.

[27] F. Smith, S. Tsynkov, E. Turkel, Compact high order accurate schemes for the three dimensional wave equation, J. Sci. Comput. 81 (2019) 1181–1209, https://doi.org/10.1007/s10915-019-00970-x.

[28] A. Zlotnik, R. Čiegis, On construction and properties of compact 4th order finite-difference schemes for the variable coefficient wave equation, J. Sci. Comput. 95 (2023) 3, https://doi.org/10.1007/s10915-023-02127-3.

[29] I.M. Babuška, S.A. Sauter, Is the pollution effect of the FEM avoidable for the Helmholtz equation considering high wave numbers?, SIAM Rev. 42 (2000) 451–484 (electronic). Reprint of SIAM J. Numer. Anal. 34 (6) (1997) 2392–2423, MR1480387 (99b:65135).

[30] A. Bayliss, C.I. Goldstein, E. Turkel, On accuracy conditions for the numerical computation of waves, J. Comput. Phys. 59 (1985) 396–404.

[31] I. Versano, E. Turkel, S. Tsynkov, Fourth-order accurate compact scheme for first-order Maxwell's equations, J. Sci. Comput. (2023), submitted for publication.

[32] D.P.S.R. Alerigi, D.I. Ketcheson, B.S. Ooi, A high-order finite volume method for Maxwell's equations in heterogeneous and time-varying media, https://arxiv.org/pdf/2307.11842.pdf, arXiv:2307.11842, 2023.

[33] P.M. Morse, H. Feshbach, Methods of Theoretical Physics. 2 Volumes, International Series in Pure and Applied Physics, McGraw-Hill Book Co., Inc., New York, 1953.

[34] L. Piegl, W. Tiller, The NURBS Book, second ed., Springer-Verlag, New York, NY, USA, 1996.

[35] S.V. Tsynkov, Numerical solution of problems on unbounded domains. A review, in: Absorbing Boundary Conditions, Appl. Numer. Math. 27 (1998) 465–532, https://doi.org/10.1016/S0168-9274(98)00025-7.

[36] T. Hagstrom, S. Lau, Radiation boundary conditions for Maxwell's equations: a review of accurate time-domain formulations, J. Comput. Math. 25 (2007) 305–336.

[37] B. Hanouzet, M. Sesquès, Absorbing boundary conditions for Maxwell's equations, in: Nonlinear Hyperbolic Problems: Theoretical, Applied, and Computational Aspects, Taormina, 1992, in: Notes Numer. Fluid Mech., vol. 43, Friedr. Vieweg, Braunschweig, 1993, pp. 315–322.
[38] E.H. Hirschel, W. Kordulla, Samples of Surface-Oriented Coordinate Systems, Vieweg+Teubner Verlag, Wiesbaden, 1981.
[39] J. Hao, C.-Y. Wen, Hypersonic flow over spherically blunted double cones, J. Fluid Mech. 896 (2020) A26, https://doi.org/10.1017/jfm.2020.331.
[40] S. Magura, S. Petropavlovsky, S. Tsynkov, E. Turkel, High-order numerical solution of the Helmholtz equation for domains with reentrant corners, Appl. Numer. Math. 118 (2017) 87–116, https://doi.org/10.1016/j.apnum.2017.02.013.
[41] S. Petropavlovsky, S. Tsynkov, Non-deteriorating time domain numerical algorithms for Maxwell's electrodynamics, J. Comput. Phys. 336 (2017) 1–35, https://doi.org/10.1016/j.jcp.2017.01.068.
[42] H. Qasimov, S. Tsynkov, Lacunae based stabilization of PMLs, J. Comput. Phys. 227 (2008) 7322–7345, https://doi.org/10.1016/j.jcp.2008.04.018.
[43] A.A. Reznik, Approximation of surface potentials of elliptic operators by difference potentials, Sov. Math. Dokl. 25 (1982) 543–545.
[44] A.A. Reznik, Approximation of the surface potentials of elliptic operators by difference potentials and solution of boundary-value problems, Ph.D. thesis, Moscow Institute for Physics and Technology, Moscow, USSR, 1983 (in Russian).